Two Types of Transitions to Relatively Fast Spinup in Tropical Cyclone Simulations with Weak to Moderate Environmental Vertical Wind Shear

David A. Schecter[1*]

[1]*NorthWest Research Associates, Boulder, Colorado, USA*

Submitted to *Journal of the Atmospheric Sciences* November 21, 2023; accepted May 16, 2024

DOI reserved for the published journal article with final edits: 10.1175/JAS-D-23-0223.1

*Corresponding author address: NorthWest Research Associates, 3380 Mitchell Lane, Boulder, CO, USA, 80301. E-mail: schecter@nwra.com

This unofficial preprint (slightly updated on August 7, 2024) is subject to minor corrections before publication.

ABSTRACT: Tropical cyclone intensification is simulated with a cloud resolving model under idealized conditions of constant SST and unidirectional environmental vertical wind shear maximized in the middle troposphere. The intensification process commonly involves a sharp transition to relatively fast spinup before the surface vortex achieves hurricane-force winds in the azimuthal mean. The vast majority of transitions fall into one of two categories labeled S and A. Type S transitions initiate quasi-symmetric modes of fast spinup. They occur in tropical cyclones after a major reduction of tilt and substantial azimuthal spreading of inner-core convection. The lead-up also entails gradual contractions of the radii of maximum wind speed (r_m) and maximum precipitation. Type A transitions begin before an asymmetric tropical cyclone becomes vertically aligned. Instead of enabling the transition, alignment is an essential part of the initially asymmetric mode of fast spinup that follows. On average, type S transitions occur well-after and type A transitions occur once the cyclonically rotating tilt vector becomes perpendicular to the shear vector. Prominent temporal peaks of lower tropospheric CAPE and low-to-midlevel relative humidity averaged over the entire inner core of the low-level vortex characteristically coincide with type S but not with type A transitions. Prominent temporal peaks of precipitation and midlevel vertical mass-flux in the meso-β scale vicinity of the convergence center characteristically coincide with type A but not with type S transitions. Despite such differences, in both cases the transitions tend not to begin before the distance between the low-level convergence and vortex centers divided by r_m reduces to unity.

1. Introduction

Tropical cyclones generally exist in environments with some degree of vertical wind shear. Although vertical wind shear tends to hinder intensification (DeMaria 1996; Gallina and Velden 2002; Tang and Emanuel 2012), a small to moderate level does not prohibit a weak tropical cyclone from eventually gaining strength. One realistic scenario is for such a tropical cyclone to experience a sharp transition from slow to relatively fast spinup on its way to becoming a hurricane. The present study investigates the changes that must take place within a tropical cyclone for such a transition to occur in cloud resolving simulations.

Previous studies have suggested that slow intensification is often linked to a shear-induced horizontal separation of the low-level and midlevel vortex centers, which is commonly referred to as a *misalignment* or *tilt* of the tropical cyclone. A substantial misalignment generally coincides with a concentration of inner-core convection far downtilt[1] from the center of the surface circulation (Stevenson et al. 2014; Nguyen et al. 2017; Fischer et al. 2024), where it is theoretically inefficient in driving spinup (Schecter 2020; cf. Vigh and Schubert 2009; Pendergrass and Willoughby 2009). Factors apparently contributing to the detrimental downtilt localization of convection include a stabilizing warm temperature anomaly and an updraft-limiting depression of relative humidity above an area covering the central and uptilt regions of the boundary layer vortex. A number of earlier papers have illustrated how the warm anomaly and relative humidity deficit can result from subsidence of incoming middle tropospheric air (Dolling and Barnes 2012; Zawislak et al. 2016; Schecter 2022, henceforth S22). The literature has further noted that the warm anomaly goes hand in hand with the tilted vortex maintaining a state of approximate nonlinear balance (Jones 1995; DeMaria 1996; S22).

There is a common understanding that tilt-enhanced "ventilation" may either work in concert with the effects of mesoscale subsidence and thermal wind balance to hinder intensification or have a dominant role in suppressing spinup (Tang and Emanuel 2012; Riemer et al. 2010,2013; Ge et al. 2013; Riemer and Laliberté 2015; Alland et al. 2022ab; Fischer et al. 2023). To elaborate, a substantial misalignment may facilitate the intrusion of highly unsaturated environmental air

[1]"Downtilt" refers to a displacement in the general direction of the tilt vector, whereas "uptilt" refers to a displacement in the opposite direction. The "tilt vector" is the horizontal position vector of the midlevel vortex center measured from the low-level center. See Fig. 3d of section 3b.

above a large section of the surface vortex and create a situation where downdrafts (associated with precipitation) more effectively reduce the moist-entropy of boundary layer air that circulates within the inner core. Overall this can help limit the areal spread of inner-core convection and weaken that which may exist downtilt. A diminishment of downtilt convection would compound the negative effect of its outward displacement on the ability of a tropical cyclone to strengthen.

The preceding discussion suggests that a sufficient reduction of tilt could eliminate the principal impediments to intensification and enable a transition to relatively fast spinup. Accordingly, a number of published studies have identified alignment as a typical precursor to a substantial acceleration of intensification (Zhang and Tao 2013; Munsell et al. 2017; Miyamoto et al. 2018; Rios-Berrios et al. 2018; Alvey et al. 2020; S22). One obvious avenue for reducing tilt is reducing the vertical wind shear to a negligible level so as to permit the tropical cyclone to freely align (Reasor et al. 2001; Schecter and Montgomery 2003,2007; Schecter and Menelaou 2020). However, tropical cyclones often have the capacity to align even if the wind shear persists at moderate strength. Various modeling studies have suggested that alignment amid moderate shear is facilitated by cyclonic precession of the tilt vector to and beyond the point of becoming perpendicular to the shear direction (Rappin and Nolan 2012; Zhang and Tao 2013; Tao and Zhang 2014; Finocchio et al. 2016; Onderlinde and Nolan 2016; Rios-Berrios et al. 2018). Among other considerations, precession of the tilt vector from a downshear to upshear orientation coincides with the neutralization and subsequent reversal of shear-related misalignment forcing (Jones 1995; Reasor et al. 2004; Schecter 2016). On the other hand, a major reduction of tilt in moderate shear does not necessarily require precession. For example, a tropical cyclone may align by "core (or center) reformation" even when the tilt vector points directly downshear (Molinari et al. 2004; Molinari and Vollaro 2010; Nguyen and Molinari 2015; Chen et al. 2018; Rogers et al. 2020; Alvey et al. 2022; Stone et al. 2023; Schecter 2023). The process generally entails strong convergence near vigorous downtilt convection causing a subvortex to strengthen underneath the central region of the midlevel vortex to the extent of becoming the new inner core of the low-level circulation. The pathways and time scales of alignment are clearly diverse, and they continue to be studied as part of an ongoing effort to better understand the timing for the onset of fast spinup.

That being said, some modeling and observational studies have suggested that alignment is not a prerequisite for a transition to relatively fast intensification (Chen and Gopalakrishnan 2015; Alvey and Hazelton 2022). The present study will corroborate those just referenced and investigate what apart from the initial tilt magnitude differentiates transitions that occur before and after alignment. Post-alignment transitions have been shown to commonly occur after pronounced enhancements of lower-to-middle tropospheric relative humidity (Chen et al. 2019; Alvey et al. 2020; S22) and lower tropospheric CAPE (S22) averaged over the inner-core of the surface vortex. Moreover, they generally follow appreciable azimuthal spreading of precipitation (Chen et al. 2019,2021; Alvey et al. 2020; Rios-Berrios et al. 2018) and initiate a quasi-symmetric mode of intensification similar to that which may exist in a shear-free system (Montgomery and Smith 2014). Since the preceding features are coupled to the reduction of the tilt magnitude, they are not expected to be characteristics of transitions that occur before alignment. A number of the distinct thermodynamic and convective features of a prealignment transition and the highly asymmetric— but reasonably efficient —mode of intensification that immediately follows will be illustrated herein.

In short, the central contribution of this paper is the exposition of a binary classification system for transitions from slow to fast spinup that are found within a large and diverse set of tropical cyclone simulations. As explained above, the two classes of transitions are distinguished by the coinciding state of misalignment and the distinct mode of intensification that follows. Both prealignment and post-alignment transitions will be seen to occur over a wide range of SSTs and during times of either weak or moderate environmental vertical wind shear. Similarities and differences between the present tilt-based classification of transitions to fast spinup and other binary conceptualizations of the process contained in earlier studies (Holliday and Thompson 1979; Harnos and Nesbitt 2011,2016ab; Judt et al. 2023) will be addressed after details of the former are expounded. Limitations of the binary classification system will also be discussed.

An important clarification is necessary before proceeding to discussions of methodologies and results. The concept of fast intensification employed for this study is broader than conventional definitions of rapid intensification (Kaplan et al. 2010; Li et al. 2022) in having no explicit minimum rate. Instead, fast intensification need only occur at a greater rate than a specified multiple of the preceding slow intensification rate (see section 2b). The probability of fast intensification considered in this relative sense under given environmental conditions may thus differ considerably from that of conventional rapid intensification (Kaplan and DeMaria 2003; Hendricks et al. 2010).

The remainder of this paper is organized as follows. Section 2 describes the essential features of the tropical cyclone simulations, and explains the method used to identify transitions from slow to fast spinup. Section 3 demonstrates that the transitions generally fall into one of two well-separated categories chiefly distinguished by the coinciding state of vertical alignment. The kinematic and moist-thermodynamic features coinciding with the distinct tilt magnitudes of tropical cyclones during each type of transition are described, and the relevance of these features to enabling fast spinup is discussed. Section 4 qualitatively compares the results of section 3 to observed transitions to fast spinup in natural tropical cyclones. Section 5 summarizes all of the main findings of this study.

2. Methodology

2.a Computational Data Set

The tropical cyclones considered herein are from a heterogeneous set of roughly one hundred simulations conducted with Cloud Model 1 (CM1; Bryan and Fritsch 2002) for a variety of purposes including the present study. Heterogeneity of the computational data set is considered beneficial by reducing (but not eliminating) methodological bias in the search for different types of transitions from slow to fast spinup.

While diverse, the simulations do have a number of basic features in common. To begin with, all simulations are conducted on a doubly-periodic oceanic f-plane at 20^oN, with the Coriolis parameter f equaling 5×10^{-5} s^{-1}. The sea surface temperature (SST) is generally held constant in space and time. The initial environmental vertical temperature and relative humidity distributions above the sea surface are taken from the Dunion (2011) moist tropical sounding for hurricane season over the Caribbean Sea.

The physics parameterizations are fairly conventional. Each simulation incorporates a variant of the two-moment Morrison cloud-microphysics module (Morrison et al. 2005,2009), having graupel as the large icy-hydrometeor category and a constant cloud-droplet concentration of 100 cm^{-3}. Radiative transfer is accounted for by the NASA-Goddard parameterization scheme (Chou and Suarez 1999; Chou et al. 2001). The influence of subgrid turbulence above the surface is accounted for by an anisotropic Smagorinsky-type closure analogous to that described by Bryan and Rotunno (2009). The horizontal mixing length l_h in each simulation increases linearly from 100 to 700 m as the surface pressure decreases from 1015 to 900 hPa. The asymptotic vertical mixing length l_v is 50 m in most simulations but 70 m in a few. Surface fluxes are parameterized with bulk-aerodynamic formulas. The momentum exchange coefficient C_d increases from a minimum of 10^{-3} to a maximum of 0.0024 as the surface (10-m) wind speed increases from 5 to 25 m s^{-1} (compare with Fairall et al. 2003 and Donelan et al. 2004). The enthalpy exchange coefficient is given by $C_e = 0.0012$ roughly based on the findings of Drennan et al. (2007). Heating associated with frictional dissipation is activated. Rayleigh damping is imposed above an altitude of $z = 25$ km.

The equations of motion are discretized on a stretched rectangular grid that spans 2660 km in each horizontal dimension and 29.2 km in the vertical dimension. The 800×800 km^2 central region of the horizontal mesh that contains the broader core of the tropical cyclone has uniform increments of 2.5 km; at the four corners of the mesh, the increments are 27.5 km. The vertical grid has 40 or 50 levels spaced 100 or 50 m apart near the surface, but farther apart aloft. When the number of levels N_z is 40 (50), the vertical grid spacing gradually grows to 0.7 and 1.4 km (0.6 and 1.1 km) as the height above sea level z increases to 8 and 29 km.

The vast majority of simulations are initialized with the nominal pre-depression (PD) vortex depicted in Fig. 1 of Schecter and Menelaou (2020). The azimuthal velocity v of the PD vortex has a maximum value of 6.1 m s^{-1} located 3 km above the sea surface, at a radius r of 140 km from the central axis of rotation. The maximum of v on the lowest model level is 4.1 m s^{-1}. Moving outward (upward) from its peak, v gradually decays until reaching zero at $r = 750$ ($z = 10.5$) km. The relative humidity in the core of the PD vortex is moderately enhanced relative to the environment. A small number of simulations are initialized with a modified Rankine (MR) vortex, corresponding to “iinit = 7” in the CM1 (release 21.0) configuration file. For these cases, v has a maximum value of 15 m s^{-1} at $r = 75$ km on the lowest model level. Moving outward (upward) from its peak, v gradually decays until reaching zero at $r = 500$ ($z = 15$) km. Both the PD and MR vortices are introduced in balanced axisymmetric states. While many (but not all) of the vortices are slightly perturbed with quasi-random noise in the lower potential temperature and water vapor fields, none are initially perturbed with coherent mesoscale asymmetries (cf. Nolan et al. 2023).

The principal differences between the simulations are in their SSTs and environmental shear flows. The SSTs range from 26 to 32 ^{o}C. In general, the environmental shear flows are horizontally uniform and strictly zonal. Their diversity comes from variations of intensity, primary shear-layer characteristics, and time-dependence.

The ground-relative velocity field of the applied environmental shear flow is given by $u_s\hat{\mathbf{x}}$, in which $\hat{\mathbf{x}}$ is the horizontal unit vector pointing eastward, and

$$u_s(z,t) = \frac{U_s}{2}\tanh\left(\frac{z-z_\alpha}{\delta z_\alpha}\right)\left[1+\tanh\left(\frac{z_\beta - z}{\delta z_\beta}\right)\right]\Upsilon(t). \tag{1}$$

In the preceding formula, U_s (0-5.6 m s^{-1}) is an adjustable constant equaling roughly one-half the nominal shear strength, z_α (5 or 5.5 km) is the center of the primary shear layer where the velocity field changes direction, δz_α (2.5 or 3.5 km) is the half-width of the primary shear layer, and z_β (21 km) is the upper altitude at which the shear flow decays toward zero with increasing height over a lengthscale δz_β of 1 km. The factor Υ depends on time t and can be varied to diversify the structural evolutions of tropical cyclones before they undergo transitions to fast spinup at a given shear strength. The most general form of Υ is given by

$$\Upsilon \equiv \begin{cases} 0 & t \leq \tau_\uparrow, \\ (t-\tau_\uparrow)/\delta\tau_\uparrow & \tau_\uparrow < t \leq \tau_\uparrow + \delta\tau_\uparrow \quad \text{(ramp up)}, \\ 1 & \tau_\uparrow + \delta\tau_\uparrow < t \leq \tau_\downarrow, \\ 1-\varepsilon_\downarrow(t-\tau_\downarrow)/\delta\tau_\downarrow & \tau_\downarrow < t \leq \tau_\downarrow + \delta\tau_\downarrow \quad \text{(ramp down)}, \\ 1-\varepsilon_\downarrow & t > \tau_\downarrow + \delta\tau_\downarrow, \end{cases} \tag{2}$$

in which $0 \leq \varepsilon_\downarrow \leq 1$. The preceding formula permits ramp-up (at $\tau_\uparrow$) and partial ramp-down (at $\tau_\downarrow$) of the shear flow. The duration of the ramp-up (ramp-down) period is $\delta\tau_\uparrow$ ($\delta\tau_\downarrow$). In general, a forcing term of the form

$$\mathbf{F}_s \equiv \frac{\partial u_s}{\partial t}\hat{\mathbf{x}} + f u_s \hat{\mathbf{z}}\times\hat{\mathbf{x}} \tag{3}$$

must be added to the horizontal velocity equation to introduce the shear flow and maintain its orientation.[2] A number of simulations have $\tau_\uparrow = 0$, $\delta\tau_\uparrow \to 0$ and $\tau_\downarrow \to \infty$ (or $\varepsilon_\downarrow = 0$). This amounts to superimposing the environmental shear flow (with $\Upsilon = 1$) onto the initial condition of the simulation and setting $\partial u_s/\partial t$ to zero in Eq. (3). Simulations with nonzero $\tau_\uparrow$ generally have

[2]In nature, the second term on the right-hand side of Eq. (3) would be associated with a meridional potential temperature gradient. Such a gradient is neglected herein to permit periodic boundary conditions, as in many previous studies. The reader may consult Nolan (2011) for an evaluation of this approach to simulating tropical cyclones.

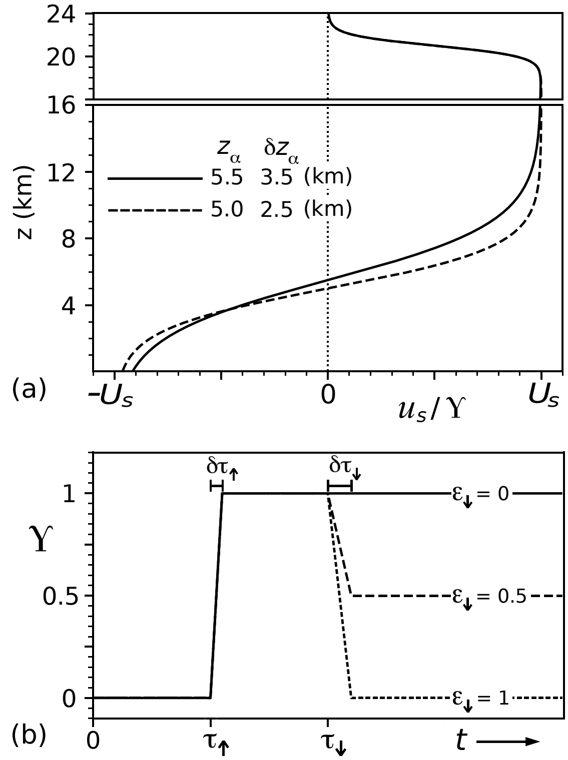

FIG. 1: (a) Vertical profiles of the environmental shear flow [u_s/Υ given by Eq. (1)] with two slightly different parameterizations of the primary shear layer used for the simulations at hand. (b) Time dependence of the shear flow [Υ given by Eq. (2)] with various ramp-down coefficients ($\varepsilon_\downarrow$) as indicated on each line.

$\delta\tau_\uparrow$ set to 1 h, and simulations with finite $\tau_\downarrow$ generally have $\delta\tau_\downarrow$ set to 3 h. The nominal 0-12 km vertical wind shear mentioned throughout the remainder of this paper corresponds to the difference between u_s evaluated at $z = 12$ and 0 km. Bear in mind that the actual deep-layer vertical wind shear in a simulation deviates slightly from this estimate owing to the effects of friction among other factors.

Figure 1 illustrates the environmental shear flows described above and used herein. While these shear flows are essentially within the spectrum of those employed in earlier modeling studies of tropical cyclone intensification, one might imagine an infinite number of realistic alternatives. The literature suggests that the timing of fast spinup and details of the viable pathways to its onset could differ with the use of alternative shear flows in which u_s has an additional constant that reverses the surface velocity (Rappin and Nolan 2012), δz_α is appreciably shortened (Finocchio et al. 2016), z_α is shifted to a substantially different altitude (ibid.; Ryglicki et al. 2018ab), or the wind direction rotates with height (Onderlinde and Nolan 2016; Gu et al. 2019).

The reader may consult appendix A for a more detailed account of the simulations examined for this study. Table A1 contained therein conveniently summarizes the variation of shear flow parameters considered at each SST, for both PD-type and MR-type initial vortex conditions. Computational nuances pertinent to certain simulation groups— and possibly relevant to reproducibility —are also addressed.

2.b Identification of Substantial Transitions from Slow to Fast Spinup

Let $\bar{v}$ denote the azimuthally averaged tangential velocity of the tropical cyclone in a polar coordinate system whose origin lies on the center of the low-level vortex ($\mathbf{x}_{cl}$ of section 3). The intensity of the vortex is defined herein as the maximum of $\bar{v}$ that is found 10 m above the sea surface, and is denoted by $V_m(t)$. The intensification rate (IR) is thus defined by dV_m/dt. In general, V_m is obtained from hourly simulation output, and dV_m/dt is computed (to second-order) from that output.

A substantial transition from slow to fast spinup is said to occur at the time t_* when two main criteria are met. First, dV_m/dt must begin a well-defined enhancement period during which its average positive value exceeds a specified multiple of the preceding IR averaged over a specified lead time. Second, the change of V_m during the enhancement period must exceed a certain threshold. Appendix B2 provides further details of the transition identification scheme. Bear in mind that the pretransitional IR is not explicitly required to fall below an absolute maximum, and the post-transitional IR is not explicitly required to exceed an absolute minimum. As mentioned earlier, intensification is considered "slow" before and "fast" after a transition in a relative sense.

Of further note, the forthcoming analysis only considers transitions that occur after a depression has formed and before the azimuthal-mean surface vortex achieves minimal hurricane intensity, marked by when $V_m = 32.5$ m s^{-1}. Not all simulated tropical cyclones in the data set used for this study were found to exhibit substantial transitions from slow to fast spinup during this developmental time frame (see Table A1).

3. Results

The present section of this paper examines the characteristics of substantial transitions from slow to fast spinup in the tropical cyclone simulations at hand. Discussion of how the results relate to observed tropical cyclone dynamics is mostly deferred to section 4.

3.a Bimodal Distribution of Tropical Cyclone Asymmetry at the Transition Time

One striking feature of the simulated transitions from slow to fast spinup is a virtually bimodal distribution of tropical cyclone symmetry during the transition period. Figure 2 shows a scatter plot of the transitional values of two asymmetry parameters. The first asymmetry parameter is the normalized tilt magnitude defined by

$$\mu \equiv \frac{|\mathbf{x}_{cu} - \mathbf{x}_{cl}|}{r_m}, \tag{4}$$

in which $\mathbf{x}_{cl}$ and $\mathbf{x}_{cu}$ respectively represent the horizontal position vectors of the low-level and midlevel (upper middle-tropospheric) vortex centers. Whereas $\mathbf{x}_{cl}$ is measured in the boundary layer, $\mathbf{x}_{cu}$ is measured roughly 8 km above sea level (see appendix B1 for details). The denominator r_m on the right-hand side of Eq. (4) is the radius of maximum $\bar{v}$ in the boundary layer. The second plotted parameter is the precipitation asymmetry [$P_{\text{asym}}(t;d)$] defined by Eq. (3) of S22 and shown to be qualitatively consistent with an alternative metric for convective asymmetry in appendix C1. In essence, P_{asym} measures the asymmetry of the quadrantal distribution of the 2-h precipitation rate in a disc of radius d [here set to $1.2r_m(t)$] centered at $\mathbf{x}_{cl}(t)$. A value of 0 indicates that the precipitation is distributed uniformly in azimuth around the disc, whereas a value of 1 indicates that the precipitation is completely confined to a single quadrant of the disc; i.e., higher values correspond to greater azimuthal asymmetry in the 2-h inner-core precipitation field. Note that an asterisk appears on each axis label of Fig. 2 to indicate that the plotted parameter is evaluated during the nominal transition period; in general, G^* is used throughout this paper to represent the 6-h time average of the generic variable G immediately after t_*. A minor deviation from this rule is used in calculating μ^* as the aforementioned time average of the numerator $|\mathbf{x}_{cu} - \mathbf{x}_{cl}|$ over that of the denominator r_m.

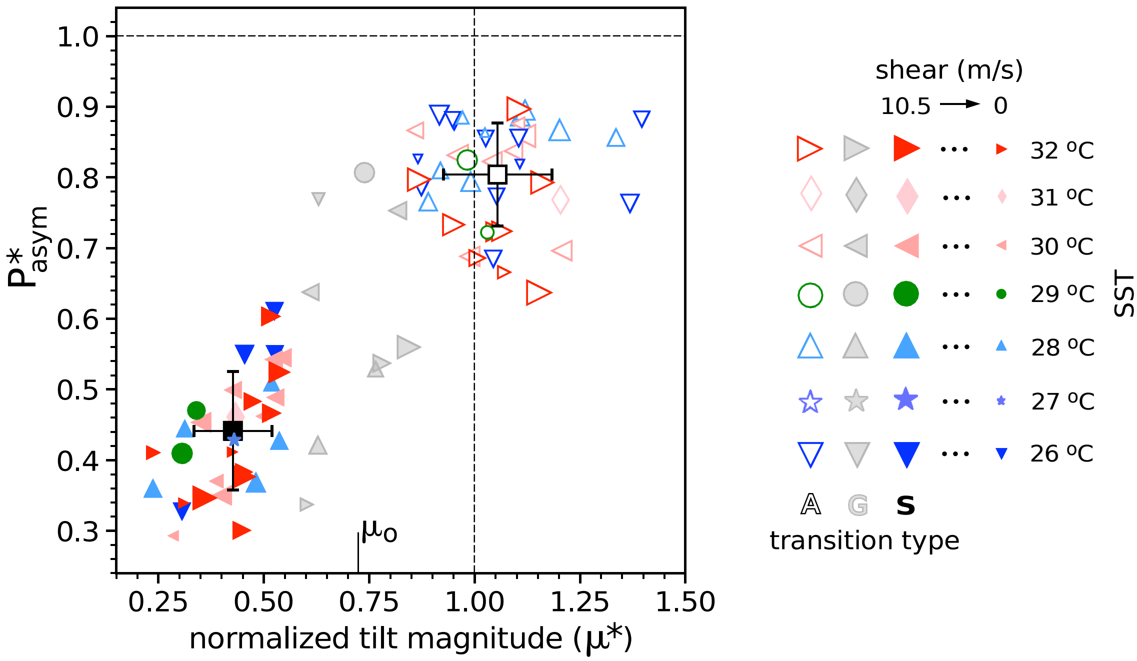

FIG. 2: Transitional values of the precipitation asymmetry (P^*_{asym}) and normalized tilt magnitude (μ^*). As shown in the legend, color-filled, empty color-edged, and gray symbols respectively represent systems that undergo type S ($\mu^* < 0.6$), type A ($\mu^* > 0.85$), and type G ($0.6 \leq \mu^* \leq 0.85$) transitions. The black and white squares respectively show the means for the S and A groups; the attached "error bars" have lengths of one standard deviation in each direction. Symbol shapes (and colors for the S and A groups) indicate the sea surface temperature. The symbol size decreases linearly with the magnitude of the 0-12 km environmental vertical wind shear at t_*; zero-shear cases correspond to a subset of the simulations with $\tau_\downarrow + \delta\tau_\downarrow < t_*$ and $\varepsilon_\downarrow = 1$ (see section 2a).

The scatter plot shows that during the transition from slow to fast spinup, the projections of the tropical cyclone state vectors onto the μ-P_{asym} plane fall largely into one of two clusters, representing relatively symmetric (S) and asymmetric (A) conditions. Tropical cyclones in the S-cluster (color-filled symbols) are characterized by $\mu^* = 0.43 \pm 0.09$ and $P^*_{\text{asym}} = 0.44 \pm 0.08$, each expressed as the cluster-mean ± one standard deviation. Tropical cyclones in the A-cluster (empty symbols) are characterized by $\mu^* = 1.05 \pm 0.13$ and $P^*_{\text{asym}} = 0.80 \pm 0.07$. Rather than using ellipses to serve as the formal boundaries of each cluster, it is deemed adequate for the present data set to differentiate the clusters according to the value of the normalized tilt magnitude (μ^*) alone. Specifically, let us define type S transitions to have $\mu^* < \mu_o - \delta\mu_o$ and type A transitions to have $\mu^* > \mu_o + \delta\mu_o$, in which $\mu_o = 0.725$ and $\delta\mu_o = 0.125$. This leaves a small number of cases (gray symbols) in the gap between the principal two transition types; they will be called gray-area (type G) transitions and generally excluded from analysis.

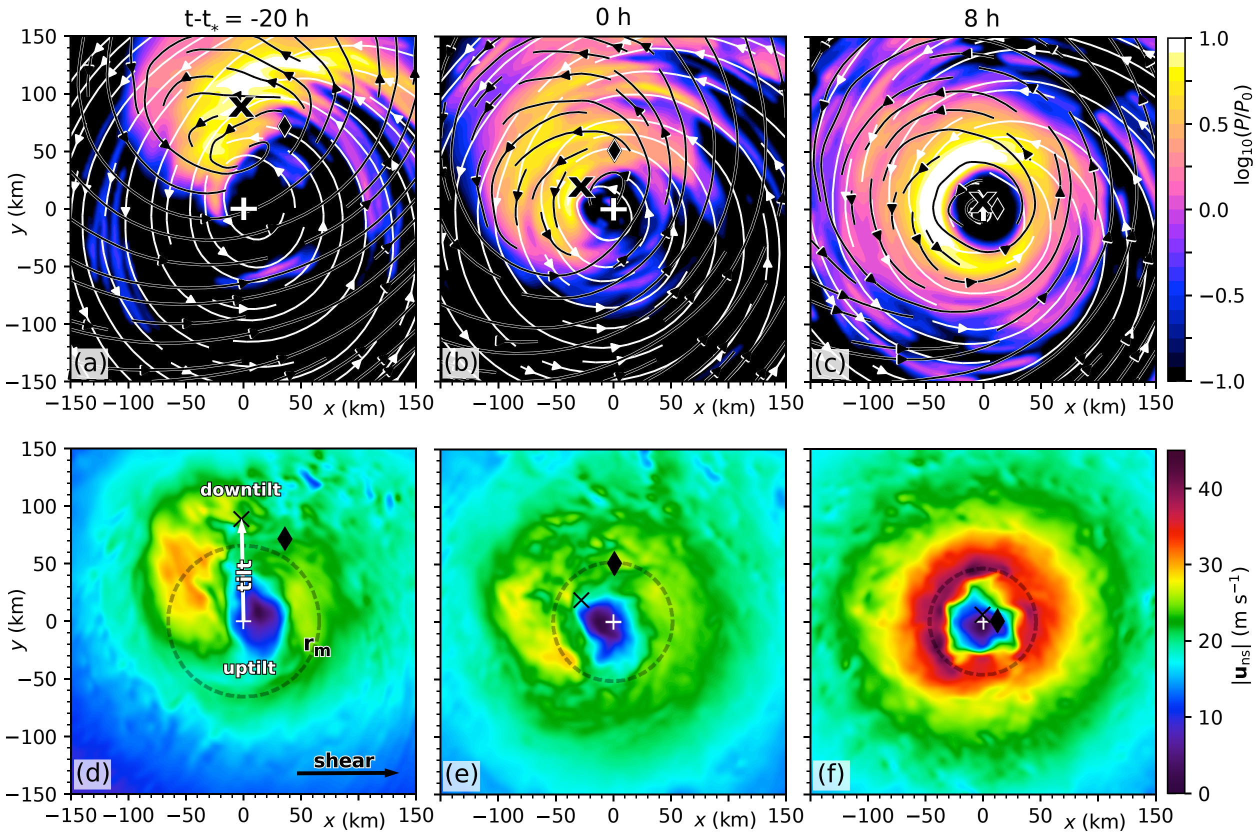

FIG. 3: Snapshots of the evolution of a tropical cyclone that undergoes a type S transition to relatively fast spinup. (a) Streamlines of the horizontal velocity fields in the approximate 1-km deep boundary layer (white) and 1-km deep middle tropospheric layer centered 8 km above sea level (black with white trim) superimposed over the base-10 logarithm of the 2-h precipitation rate P normalized to $P_0 = 0.375$ cm h^{-1} (color), 20 h before the transition time t_*. (b,c) As in (a) but for (b) $t = t_*$ and (c) $t = t_* + 8$ h. (d) Magnitude of the near-surface ($z = 50$ m) horizontal velocity field $\mathbf{u}_{ns}$ at the pretransitional time of (a). (e,f) As in (d) but at (e) t_* and (f) $t_* + 8$ h. In all panels, the + marks the low-level vortex center $\mathbf{x}_{cl}$, the $\times$ marks the midlevel vortex center $\mathbf{x}_{cu}$, and the diamond marks the low-level convergence center $\mathbf{x}_{\sigma}$ defined in appendix B1. In (d), the white arrow shows the tilt vector, and the black arrow points in the direction of the environmental vertical wind shear. The dashed circle in (d-f) that is centered on $\mathbf{x}_{cl}$ and has a radius of r_m demarcates the inner core of the low-level vortex. All velocity fields are relative to the surface of the earth, but the origin of the coordinate system moves with the low-level vortex center. Each velocity "snapshot" is a 2-h average.

3.b Illustrations of Selected Type S and Type A Transitions

Figure 3 illustrates the evolution of a tropical cyclone that begins a type S transition from slow to fast spinup at $t_* = 113$ h. The SST of the system is 28 ^{o}C and the 0–12 km environmental vertical wind shear is 5.4 m s^{-1}. The environmental shear flow was introduced at a time ($\tau_{\uparrow} = 54$ h) well into the development of the original PD vortex. At the first snapshot there exists a prominent

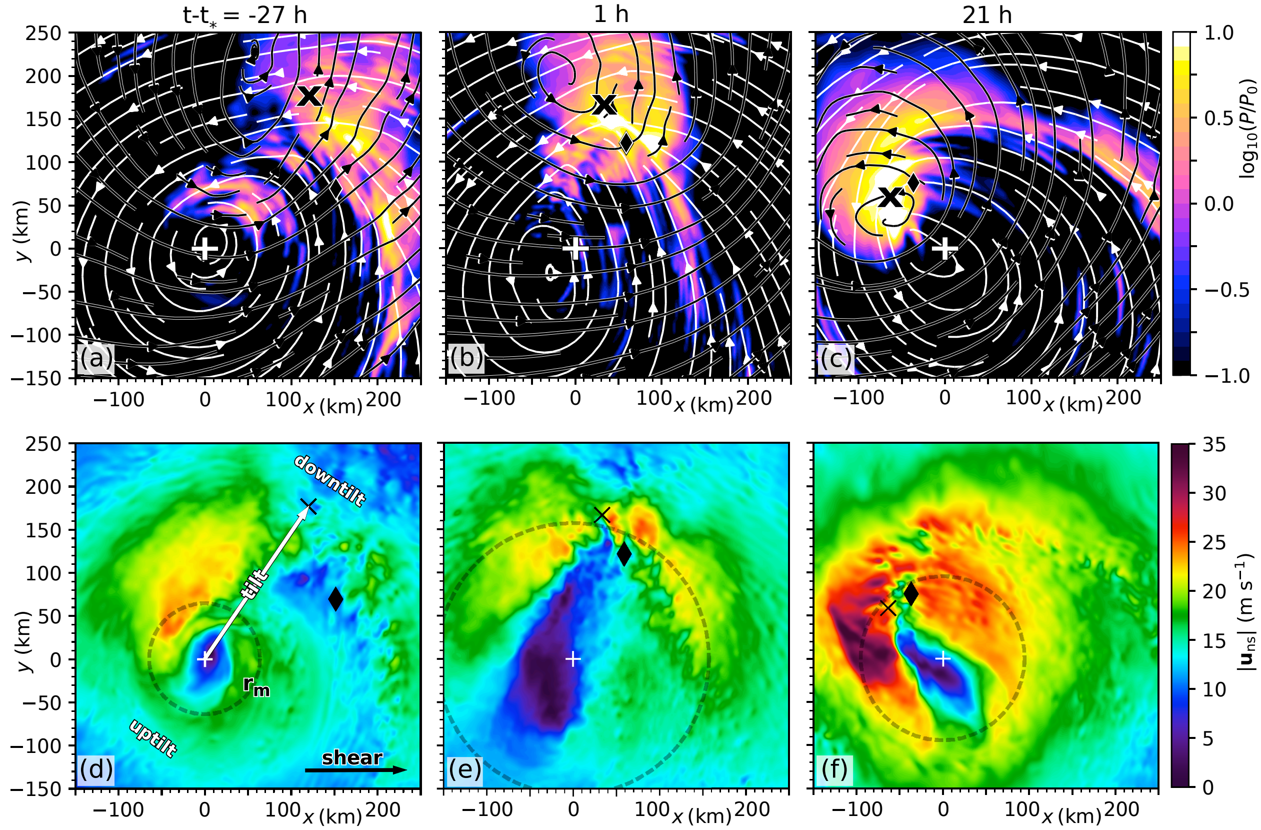

FIG. 4: Snapshots of the evolution of a tropical cyclone that undergoes a type A transition to relatively fast spinup. All panels are similar to those of Fig. 3, but the snapshots are taken at (a,d) $t_* - 27$ h, (b,e) $t_* + 1$ h and (c,f) $t_* + 21$ h. Minor differences apart from the snapshot times include extended axes, a smaller range of wind speeds in the colormap for $|\mathbf{u}_{ns}|$, and $P_0 = 0.5$ cm h^{-1}.

100-km scale horizontal displacement of the low-level and midlevel vortex centers (tilt). Deep cumulus convection and precipitation are consequently concentrated in the downtilt sector of the surface vortex, in the neighborhood of the midlevel vortex center (Fig. 3a). During this phase of slow intensification, the azimuthal-mean surface winds generally do not exceed tropical storm intensity (Fig. 3d). By the start of the transition period (Figs. 3b and 3e), the tilt of the tropical cyclone has decayed considerably and the azimuthal spread of precipitation has appreciably expanded in the vicinity of r_m. Soon after the transition period (Figs. 3c and 3f), a relatively fast quasi-symmetric mode of intensification is well underway.

Figure 4 shows selected snapshots of the evolution of a tropical cyclone that begins a type A transition at $t_* = 124$ h. The simulation is conducted as before but with a greater 0–12 km environmental vertical wind shear of 7.3 m s^{-1} combining with the moderate (28^{o}C) SST. The tilt generated by the larger wind shear is found to equal or exceed 170 km roughly 1 d before (Fig. 4a) and during (Fig. 4b) the transition to fast spinup. For the same times, the peak region of downtilt convection has a comparable displacement from the low-level vortex center. The initial smallness of the radius of maximum surface wind speed r_m comes from an earlier time of less tilt and more prominent inner convection. The growth of r_m from 64 km in Fig. 4d to 157 km in Fig. 4e starts in earnest after a momentary lull of outer convection, reinvigoration of inner convection, and reduction of the tilt magnitude (not shown). The subsequent regrowth of tilt and coupled enhancement of outer convection coincide with the expansion of r_m. During the early-to-intermediate phase of post-transitional intensification (Figs. 4c and 4f), the tilt magnitude and r_m decay to an extent, but convection and precipitation remain focused in the downtilt sector of the surface vortex. Of further note, while the post-transitional IR substantially exceeds the slightly negative IR existing prior to t_*, it is measurably smaller than that found after the type S transition considered above; the 24-h post-transitional IRs in the present and previous examples are respectively 0.4 and 1.0 m/s h^{-1}. Forthcoming analysis will examine the qualitative generality of this disparity.

3.c Intensity and IR Differences Between Systems that Experience Type S and Type A Transitions

Figure 5 shows composite time series of (a) V_m and (b) dV_m/dt for tropical cyclones that experience type S (red) and type A (blue) transitions. In an effort to reduce SST-related variability (Emanuel 1986; Črnivec et al. 2016; Xu et al. 2016,2019; Xu and Wang 2018), V_m is normalized to an estimate of the maximum potential intensity $V_{\max}$ (see appendix B3), and dV_m/dt is normalized to the following theoretical estimate of the maximum potential intensification rate adapted from Wang et al. (2021):

$$\mathrm{MPIR} = \frac{27}{256}\frac{\alpha C_d}{h}V_{\max}^2, \tag{5}$$

in which $\alpha = 0.75$ ostensibly represents the ratio of 10-m to boundary-layer maximum wind speeds, $h = 2000$ m is an effective depth of the boundary layer, and $C_d = 0.0024$ is the value of the surface drag coefficient in the vicinity of r_m when $V_m = V_{\max}$. To further reduce variability with the ocean temperature, $t - t_*$ is normalized to $\tau_e \equiv V_{\max}/\mathrm{MPIR}$, which represents an SST-dependent "minimum" time scale for complete intensification (evolution to maximal strength). Each dark curve in Fig. 5 represents the mean for all simulations with a transition of the type indicated by its color. The light semi-transparent shading surrounding each dark curve extends vertically from the 20$^{\text{th}}$ to 80$^{\text{th}}$ percentile for the color-matched simulation group. Data from any

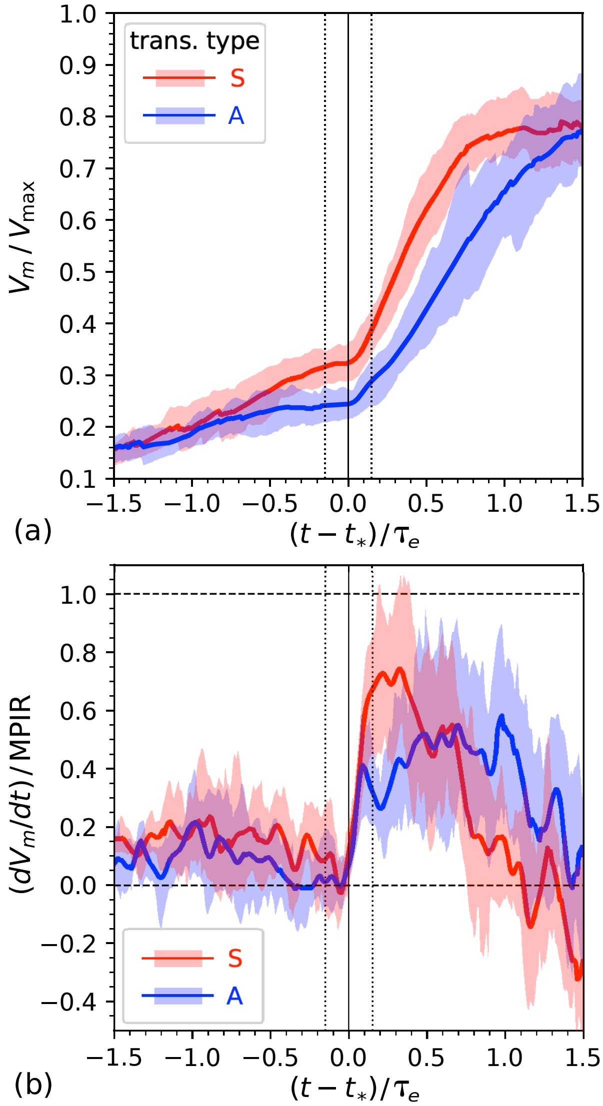

FIG. 5: Time series of (a) the maximum 10-m azimuthal velocity V_m normalized to the maximum potential intensity and (b) the intensification rate normalized to the MPIR for systems that experience type S (red) and type A (blue) transitions to relatively fast spinup. Time is measured from t_* and normalized to τ_e. Each dark solid curve shows the mean of the plotted variable for all systems in a particular transition group; the semi-transparent color-matched shading conveys the statistical spread of that variable (see the main text). Thin black-solid and black-dotted vertical lines in the two panels respectively show where $(t-t_*)/\tau_e = 0$ and ± 0.15, which approximately corresponds to $t - t_* = \pm 6$ h (9 h) when the SST is 32 ^{o}C (26 ^{o}C).

particular simulation is incorporated into the analysis only after u_s has obtained its final magnitude, and only after the tropical cyclone has been sufficiently perturbed in the sense of having achieved a tilt magnitude above 50 km. [A minority of the simulations do not meet the preceding inclusion criteria until after $t = t_* - \tau_e$. Sensitivity tests completely excluding these simulations from analysis have shown little change to the composite-mean time series presented here and elsewhere.]

environment	trans. type	V_m^* (m/s)	IR^-_{24h} (m/s h^{-1})	IR^+_{12h} (m/s h^{-1})	IR^+_{24h} (m/s h^{-1})
cool SST	S	19.4 ± 0.5	0.09 ± 0.06	0.54 ± 0.21	0.56 ± 0.11
	A	14.3 ± 2.4	0.02 ± 0.10	0.22 ± 0.09	0.29 ± 0.09
mod SST	S	21.8 ± 2.1	0.11 ± 0.07	0.71 ± 0.30	0.86 ± 0.17
	A	15.9 ± 2.1	0.00 ± 0.08	0.43 ± 0.18	0.51 ± 0.15
mod SST, low shear	S	21.7 ± 1.6	0.10 ± 0.07	0.64 ± 0.15	0.82 ± 0.13
	A	14.6 ± 2.1	0.03 ± 0.09	0.35 ± 0.07	0.44 ± 0.11
mod SST, high shear	S	22.0 ± 2.4	0.11 ± 0.06	0.78 ± 0.38	0.90 ± 0.19
	A	16.4 ± 1.8	-0.01 ± 0.07	0.47 ± 0.20	0.54 ± 0.15
warm SST	S	23.0 ± 1.7	0.26 ± 0.11	1.03 ± 0.27	0.90 ± 0.24
	A	16.1 ± 2.0	0.01 ± 0.09	0.55 ± 0.17	0.52 ± 0.15

TABLE 1. Environmental variation of tropical cyclone intensity and IR statistics for type S and type A transitions, each expressed as the mean ± 1 standard deviation for a given simulation group.

Figure 5a shows that the normalized tropical cyclone intensities during type S transitions ($V_m^*/V_{\mathrm{max}} = 0.34 \pm 0.04$) tend to be larger than those observed during type A transitions ($V_m^*/V_{\mathrm{max}} = 0.26 \pm 0.05$). Figure 5b shows that the normalized IRs tend to peak sooner (in normalized time) and higher after type S transitions than after type A transitions. The higher peaks found shortly after type S transitions seem consistent with theories suggesting that the potential for relatively large normalized IRs in weak tropical cyclones grows with the normalized wind speed [e.g., Eq. (22) of Wang et al. (2021)]. Other distinct properties of the tropical cyclones that may have greater roles in differentiating the post-transitional IRs will be addressed in due course.

For good measure, Table 1 shows the environmental variation of the dimensional values of V_m^* and three pertinent IR measurements, for both type S and type A transitions. The IR measurements include the 24-h average immediately before t_* (IR^-_{24h}), the 12-h average immediately after t_* (IR^+_{12h}) and the 24-h average immediately after t_* (IR^+_{24h}). For a relatively small number of simulations in which the environmental vertical wind shear is reduced at a time $\tau_\downarrow$ less than 24 h before t_*, the pretransitional averaging begins at $\tau_\downarrow$. Separate statistics are given for systems with cool (26-27^{o}C), moderate (28-30^{o}C) and warm (31-32^{o}C) SSTs. Table 1 also shows the variation of the transition statistics between systems with low (≤ 5 m s^{-1}) and high (> 5 m s^{-1}) environmental vertical wind shear when the SST has a moderate value.[3] The table verifies that *regardless of the environmental*

[3]Smaller data sets discourage examination of wind shear sensitivity at other SSTs (see Fig. C3).

conditions, tropical cyclones tend to be stronger during type S than during type A transitions; the azimuthal-mean surface vortices characteristically have tropical storm strength winds during transitions of type S and depression strength winds during transitions of type A. Furthermore, changing the environment does not change the general result that the mean pretransitional and post-transitional IRs are larger for type S than for type A transitions. Note also that 24-h IRs exceeding the often used rapid intensification threshold of 15 m s^{-1} per day (0.625 m s^{-1} per hour) are common immediately after type S transitions over moderate or warm oceans but uncommon immediately after type A transitions in any SST-group.

Given that substantial surface-vortex asymmetries can exist during early tropical cyclone development and generally extend beyond type A transitions, one might wonder whether the intensification curves in Fig. 5a would radically change upon replacing V_m with the absolute maximum grid value of the 10-m wind speed within the storm system. The latter metric is arguably somewhat closer to an observational standard, but does not explicitly filter out wind gusts. Appendix C2 shows that switching to the absolute maximum 10-m wind speed reduces intensification differences preceding type S and type A transitions, but essentially maintains the 1-d post-transitional disparity.

3.d Tilt Magnitude and Radius of Maximum Wind Speed

Figure 6a shows how the tilt magnitude normalized to r_m [μ defined by Eq. (4)] evolves during the time frame surrounding a transition to fast spinup. As before, separate time series are shown for systems experiencing type S and type A transitions. The disparity in the average value of μ during type S and type A transitions (Fig. 2) can be seen to extend to periods well before and well after t_*. Despite the aforementioned disparity, *both* time series hint that a pronounced drop of μ immediately preceding t_* may often help trigger the sharp acceleration of intensification that follows.

In addition to having substantially larger values of μ, tropical cyclones evolving through type A transitions generally have larger dimensional tilt magnitudes (Fig. 6b) and values of r_m (Fig. 6c) than tropical cyclones evolving through type S transitions. Previous studies have explicitly shown that both the tilt magnitude (Schecter and Menelaou 2020; Rios-Berrios 2020; Fischer et al. 2024) and r_m (Carrasco et al. 2014; Xu and Wang 2015,2018) tend to be anticorrelated to the IR of a tropical cyclone. One might therefore reasonably assume that the larger tilt and r_m of a tropical cyclone evolving through a type A transition contribute to its smaller IRs on both sides of t_* (section 3c).

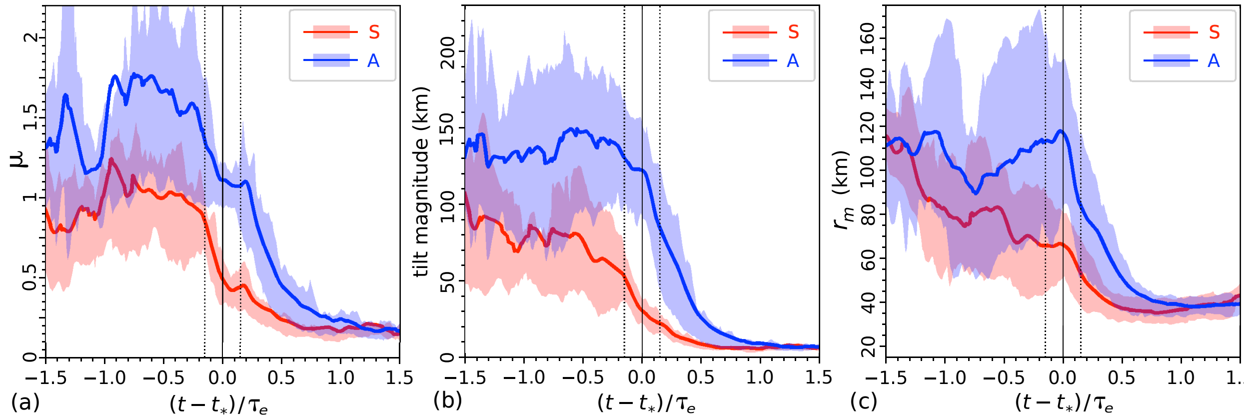

FIG. 6: Time series of (a) the normalized tilt magnitude μ, (b) the dimensional tilt magnitude $|\mathbf{x}_{cu} - \mathbf{x}_{cl}|$, and (c) the low-level radius of maximum wind speed r_m. Plotting conventions are as in Fig. 5.

Of further note, the average trends of the tilt magnitude and r_m (Figs. 6b-c) differ between systems heading toward transitions of type S or A. Shortly before type S transitions, the group mean of the tilt magnitude sharply drops while that of r_m varies little. Before type A transitions, the group mean of the tilt magnitude modestly decays while that of r_m distinctly grows. The latter result hints that core expansion may sometimes appreciably contribute to the reduction of μ toward unity prior to the onset of fast spinup in relatively asymmetric tropical cyclones.

3.e The Tilt Angle

Figure 7 shows the evolution of the angle $\varphi_{\rm tilt}$ between the tilt vector and the unit vector pointing downshear ($\hat{\mathbf{x}}$), measured counterclockwise from the latter. A few simulations in which the shear becomes zero and thus nondirectional before t_* have been removed from the analysis. In general, $\varphi_{\rm tilt}$ tends to increase leading up to either a type S or A transition. For systems undergoing type S transitions, the mean of $\varphi_{\rm tilt}$ first reaches 90^o at a time $t_\perp$ roughly equal to $t_* - 0.4\tau_e$. Accordingly, the precession of the tilt vector into a counterclockwise-perpendicular orientation relative to the shear vector does not immediately trigger fast spinup. On the other hand, $t_\perp$ approximately coincides with the onset of relatively fast alignment (Fig. 6b). For systems undergoing type A transitions, $t_\perp$ approximately coincides with the simultaneous initiation of relatively fast alignment and spinup at t_*. Although $t_* - t_\perp$ differs considerably between the two groups of tropical cyclones, the preceding results for both are essentially consistent with a number of earlier studies (see section 1) suggesting that $\varphi_{\rm tilt}$ leaving the downshear "semicircle" facilitates the acceleration of intensification.

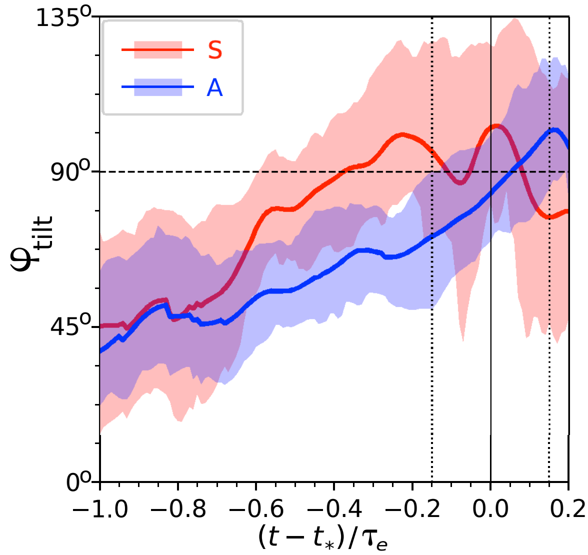

FIG. 7: Time series of the tilt angle; plotting conventions are as in Fig. 5.

3.f Tropical Cyclone Convection

Thus far the analysis has focused on differences in vortex parameters during the time frames surrounding type S and type A transitions. The following examines additional differences in various parameters associated with convection.

Figure 8a shows time series of P_{asym}, which measures the azimuthal asymmetry of the inner-core precipitation field as explained in section 3a. The precipitation asymmetry well before a type S transition [$(t-t_*)/\tau_e \approx -0.75$ to -0.15] tends to be modestly smaller than that found prior to a type A transition. A more pronounced difference begins to develop slightly before the transition point [$(t-t_*)/\tau_e \approx -0.15$], when P_{asym} precipitously drops in the type S scenario while remaining nearly constant until $t = t_*$ in the type A scenario. In the latter case, P_{asym} starts to decay in concert with alignment and contraction of r_m (Fig. 6) only after the transition officially begins.

Figure 8b shows time series of the nominal precipitation radius r_p defined as follows: Let $\bar{P}(r,t)$ denote the azimuthal average of the 2-h surface precipitation rate at a radius r from the low-level vortex center $\mathbf{x}_{cl}$; r_p is the value of r at which $\bar{P}$ is maximized. For systems undergoing either type S (red) or type A (blue) transitions, the means of r_p (thick dark curve) and r_m (thin dark curve) tend to differ little from each other over the course of time. Such behavior would seem consistent with the conventional notion that the radius of maximum wind speed is dynamically linked (with variable response lag) to the vicinity of prominent convective activity. Of particular note, the

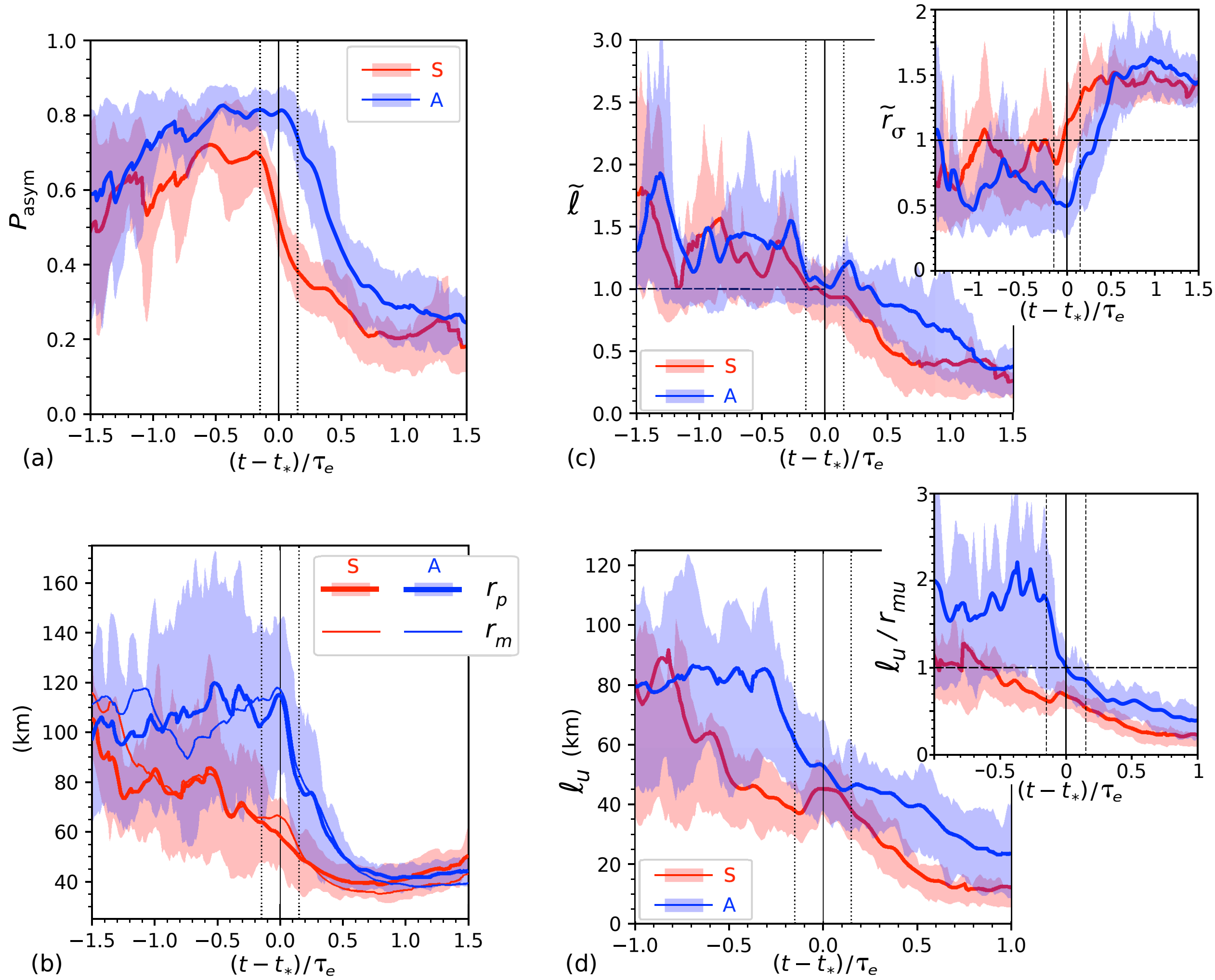

FIG. 8: Time series of parameters characterizing the spatial distributions of precipitation and low-level convergence. (a) The precipitation asymmetry P_{asym}. (b) The precipitation radius r_p (thick dark curves, light shading) compared to the mean of r_m (thin dark curves). (c) The distance ℓ between the convergence center $\mathbf{x}_\sigma$ and the low-level vortex center $\mathbf{x}_{cl}$ (main plot), and the characteristic radial lengthscale r_σ of the convergence zone (inset). Both parameters are normalized to r_m as indicated by the tildes. (d) The distance ℓ_u between $\mathbf{x}_\sigma$ and the midlevel vortex center $\mathbf{x}_{cu}$ measured in km (main plot) and normalized to r_{mu} (inset). Plotting conventions are as in Fig. 5.

close correspondence between r_p and r_m at t_* suggests that the relatively large (small) vortex cores found during type A (S) transitions coincide with relatively large (small) displacements of moist convection from $\mathbf{x}_{cl}$.

Of additional interest are the properties of the initially asymmetric low-level convergence field $\sigma_l \equiv -\nabla\cdot\mathbf{u}_l$ that is often enhanced in the vicinity of downtilt convection and plays an important role in local vertical vorticity production through the forcing term $\eta_l\sigma_l$. Here, $\mathbf{u}_l$ and η_l are the horizontal velocity field and absolute vertical vorticity in the 1-km deep boundary layer adjacent to the sea surface. Figure 8c illustrates the evolution of two parameters characterizing the spatial distribution of σ_l. The first parameter $\ell \equiv |\mathbf{x}_\sigma - \mathbf{x}_{cl}|$ is the distance between the low-level convergence and vortex centers. The convergence center $\mathbf{x}_\sigma$ is essentially the point about which the meso-β scale inflow associated with σ_l is strongest in the circumferential mean (see appendix B1). The second parameter r_σ is the radius r at which the mean radial velocity in a polar coordinate system centered at $\mathbf{x}_\sigma$ [given by the formula $\bar{u}_l(r,t) \equiv -\int_0^{2\pi} d\varphi \int_0^r dr' r' \sigma_l / 2\pi r$] has its largest negative value. The plotted time series are for the preceding parameters normalized to r_m.

Before a transition to relatively fast spinup, $\tilde{\ell} \equiv \ell / r_m$ and $\tilde{r}_\sigma \equiv r_\sigma / r_m$ respectively tend to exceed and sit below unity. The implied pretransitional positioning of a moderately compact convergence zone appreciably beyond r_m theoretically hinders intensification (Schecter 2020; cf. Vigh and Schubert 2009). By the time t_* of a type S or A transition, $\tilde{\ell}$ is generally close to 1. However, $\tilde{r}_\sigma$ differs considerably between the two categories. Consistent with greater (lesser) inner-core convective symmetry, $\tilde{r}_\sigma$ surpasses (stays well under) unity during a type S (A) transition. Eventually, $\tilde{\ell}$ declines toward zero and $\tilde{r}_\sigma$ increases toward a quasi-steady value between 1.4 and 1.5 on average for both groups of simulated tropical cyclones. Such a scenario is consistent with the progressive reorganization of the low-level convergence field into a ring-like distribution around the surface vortex center, with the associated inflow velocity peaked moderately outside of r_m.

Figure 8d further reveals that typical type A transitions are preceded by rapid contraction of the distance between the low-level convergence center and the midlevel vortex center, given by $\ell_u \equiv |\mathbf{x}_\sigma - \mathbf{x}_{cu}|$. Moreover, the mean ratio of ℓ_u to the radius of maximum wind speed r_{mu} of the midlevel vortex generally falls to unity by the onset of relatively fast spinup. One might tentatively speculate that closer proximity of $\mathbf{x}_\sigma$ to $\mathbf{x}_{cu}$ corresponds to a relatively favorable setup for strong convection around $\mathbf{x}_\sigma$, perhaps partly due to greater shielding from midlevel ventilation. That being said, ℓ_u dropping below r_{mu} does not appear to be sufficient cause for the onset of fast spinup; the inset of Fig. 8d shows that ℓ_u / r_{mu} is generally less than unity well before t_* in tropical cyclones that experience type S transitions.

Having breached the topic of convective intensity, it is now fitting to examine whether precipitation rates and vertical mass fluxes differ during transitions of type S and type A. Figures 9a-c show the evolution of the normalized 2-h surface precipitation rate P averaged within a radius R of (a) 200, (b) 100 or (c) 35 km from $\mathbf{x}_\sigma$. To limit variability associated with the amplification of

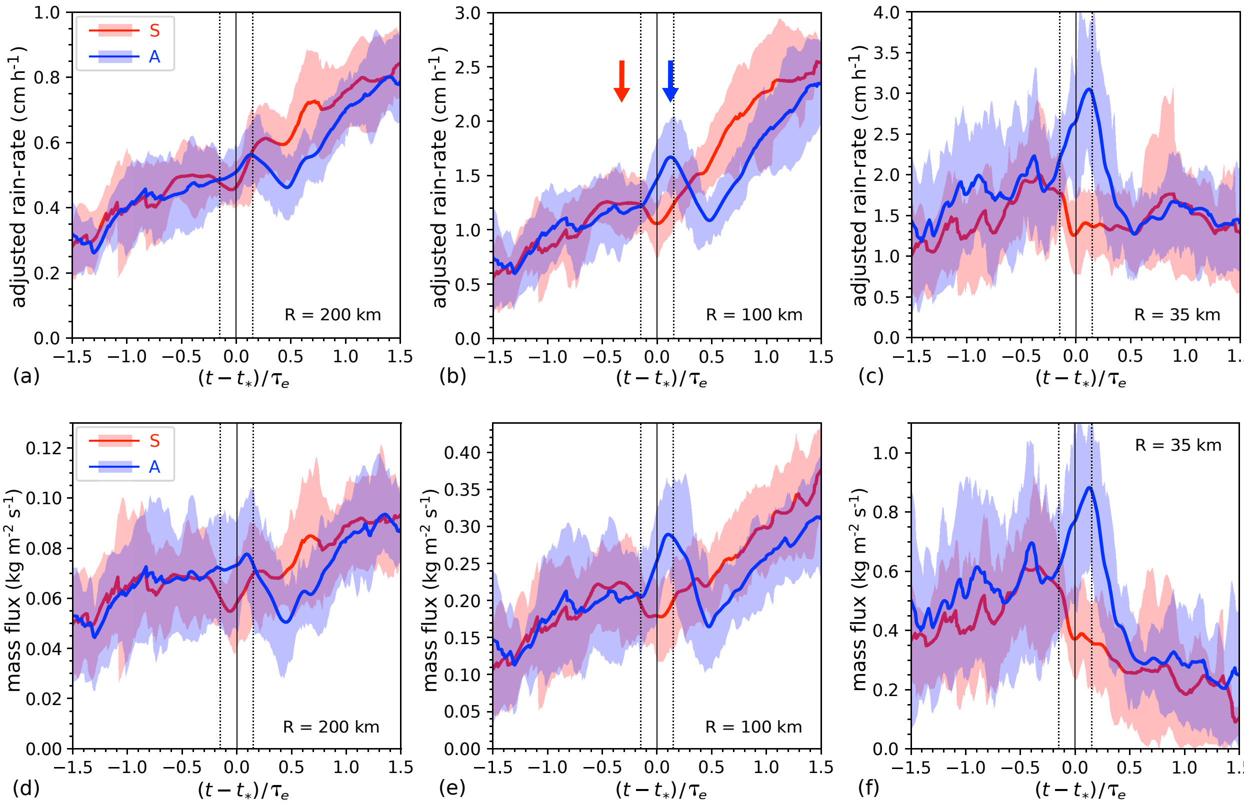

FIG. 9: Time series of parameters associated with the strength of convection. (a-c) The 2-h precipitation rate P and (d-f) the lower-middle tropospheric vertical mass flux M averaged within (a,d) 200 km, (b,e) 100 km and (c,f) 35 km of the low-level convergence center $\mathbf{x}_\sigma$. The precipitation rates in (a-c) are adjusted to compensate for increasing precipitation at higher SSTs as explained in section 3f and appendix B4. The arrows in (b) point to the initial plateau or peak phase of the secondary oscillations mentioned in the main text for the S (red) and A (blue) simulation groups. All other plotting conventions are as in Fig. 5.

precipitation as the ocean temperature warms in the model (cf. Lin et al. 2015), P is multiplied by a scaling factor ξ that increases from a base value of 1 as the SST decreases from 32^{o}C (see appendix B4). For $R = 200$ km, there is minimal difference in the steady growth of P leading up to transitions of type S or A. Upon reducing R to 100 km, a secondary oscillation becomes more noticeable, with a distinct plateau or peak (marked by an arrow for each time series in Fig. 9b) occurring shortly before or during the onset of a symmetrization trend (cf. Fig. 8a) and a trough occurring afterward. Whereas a type S transition coincides with the trough of the P-oscillation, a type A transition coincides with the peak. Upon reducing R to 35 km, so as to focus on the small-end of meso-β scale convective activity centered on $\mathbf{x}_\sigma$, the nominal oscillation becomes a major feature of the time series. Moreover, the magnitude of P during a type A transition (near t_*) corresponds to an absolute maximum that far exceeds the magnitude found during a type S transition.[4]

Figures 9d-f show complementary time series of the vertical mass flux M located 5.2–5.4 km above sea level, averaged as before within a radius R of (d) 200, (e) 100 or (f) 35 km from $\mathbf{x}_\sigma$. The composite-mean time series at other altitudes examined for z between 3 and 11 km are virtually proportional to those shown, but (for $R < 200$ km) generally decrease in magnitude from the middle to upper troposphere. Moreover, the plotted time series of M are qualitatively similar to those of P, especially when R is 100 or 35 km. Such similarity provides reasonable grounds for assuming that the aforementioned peaks and troughs of P in the vicinity of the convergence zone coincide with relatively high and low degrees of moderate-to-deep convective activity. A more detailed analysis of how P divides into contributions from various types of cumuliform and stratiform clouds is deferred to future study.

The mean drops of P and M in the vicinity of the convergence zone shortly preceding a type S transition suggest that the coinciding quasi-symmetrization is here more relevant for the switch to fast spinup than strengthening of localized convection (cf. Schecter 2022). By contrast, the pronounced peaks of P and M found in the neighborhood of the convergence zone during a type A transition suggest that exceptionally strong convection therein may be required to initiate relatively fast intensification of V_m when the tilt magnitude, r_m and ℓ are relatively large. Such would seem qualitatively consistent with previous observations of invigorated downtilt convection having an integral role in the initiation of the rapid intensification of substantially misaligned tropical cyclones; recent examples can be found in Alvey et al. (2022) and Stone et al. (2023).

3.g Moist-Thermodynamic Structure of the Tropical Cyclone

3g.1 Illustrative Examples

It is natural to ask how the convective dissimilarities between systems undergoing different types of transitions to relatively fast spinup might relate to differences in the moist-thermodynamic structure of the tropical cyclone. We shall first address this issue through illustrative examples. Figure 10 shows 2-h averages of selected moist-thermodynamic fields centered 20 h before (top row) and at

[4]The distribution of t_* measured in the time of day (0-24 h) has a fairly broad spread, suggesting no critical connection between the peak of P during type A transitions and the solar radiation cycle in the simulations at hand. The 25$^{\text{th}}$, 50$^{\text{th}}$ and 75$^{\text{th}}$ percentiles of t_* for type A transitions are respectively 9 h, 13 h and 17 h.

the start of (bottom row) a type S transition; the simulation corresponds to that in Fig. 3. The first field (left column) is the “lower tropospheric” convective available potential energy (LCAPE) introduced in S22. As defined therein, LCAPE is the vertical integral of 500-m mixed-layer parcel buoyancy assuming undiluted pseudoadiabatic ascent from the surface to the 600-hPa pressure level (z_{600}) of the atmosphere. In other words,

$$\text{LCAPE} \equiv \int_0^{z_{600}} dz\, g\, \frac{\theta_{v,\text{prcl}} - \theta_v}{\theta_v}, \tag{6}$$

in which g is the gravitational acceleration and θ_v ($\theta_{v,\text{prcl}}$) is the virtual potential temperature of the local atmosphere (ascending mixed-layer parcel). Negative and low positive values of LCAPE indicate areas where the invigoration of deep convection is theoretically improbable. The second field (middle column) is the vertical average of the relative humidity (RH) from the lower tropospheric height of 2 km to the middle tropospheric height of 8 km. The RH is defined with respect to liquid water (ice) for temperatures above (below) 0 ^{o}C. Low values of free-tropospheric RH in environments of low to moderate deep-layer CAPE (pertinent to the tropics) are thought to hinder the invigoration of deep convection where it might otherwise thrive, owing partly to the entrainment of relatively dry air into initially moist updrafts (Brown and Zhang 1997; James and Markowski 2010; Kilroy and Smith 2013). The third field θ_{el} (right column) is the equivalent potential temperature defined as in Emanuel (1994), vertically averaged over the 1-km deep boundary layer.

Well before the type S transition, the moist-thermodynamic structure of the tropical cyclone seems qualitatively consistent with expectations from past observational studies of tilted tropical storms (such as Dolling and Barnes 2012). To begin with, low and negative values of LCAPE pervade the inner core of the surface vortex, except within a downtilt sector that extends moderately upwind (Fig. 10a). Precipitation-cooled downdrafts bringing low-entropy air into the boundary layer presumably contribute substantially to the peripheral depression of LCAPE that extends appreciably downwind from the downtilt convection zone (located near the ×). However, the depression of LCAPE in the immediate and uptilt neighborhood of the low-level vortex center $\mathbf{x}_{cl}$ (marked by the +) may be mostly linked to a positive temperature anomaly in the lower free-troposphere[5] that is required to maintain approximate nonlinear balance in a tilted tropical cyclone. Otherwise, the

[5]The author has verified the existence of such a positive temperature anomaly above the central and uptilt regions of the surface vortex of the pretransitional tropical cyclone. Similar anomalies are illustrated in S22.

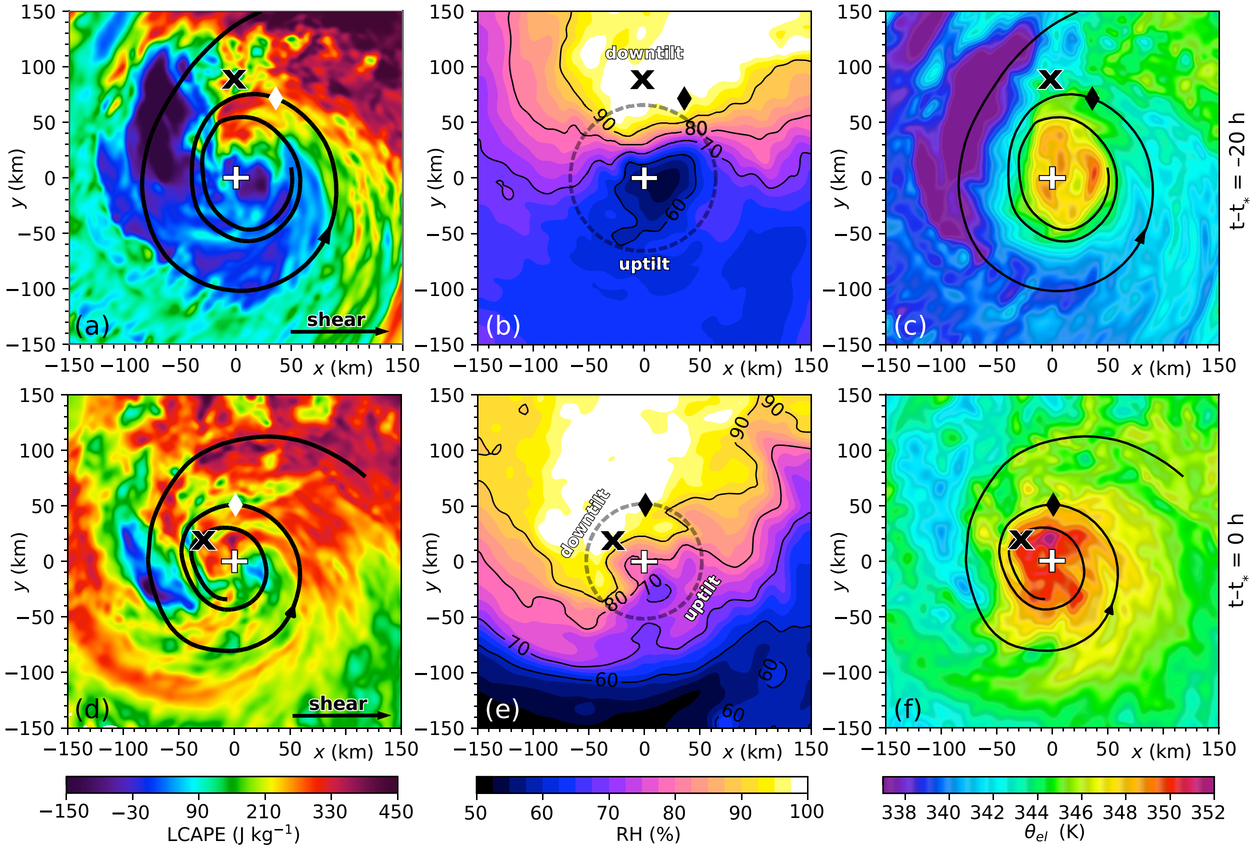

FIG. 10: Distributions of (a,d) LCAPE, (b,e) lower-to-middle tropospheric RH and (c,f) boundary layer equivalent potential temperature θ_{el} in a tropical cyclone (top row) 20 h before a type S transition begins $[(t-t_*)/\tau_e = -0.40]$ and (bottom row) at the start of the transition. The +, × and diamond respectively mark the low-level vortex center $\mathbf{x}_{cl}$, the midlevel vortex center $\mathbf{x}_{cu}$ and the convergence center $\mathbf{x}_\sigma$. The black spiral in each plot of LCAPE and θ_{el} shows the streamline of the boundary layer velocity field passing through $\mathbf{x}_\sigma$ to convey the general sense of the circulation. The dashed circles centered on $\mathbf{x}_{cl}$ in the RH plots have radii equal to r_m.

depression would seem inconsistent with the presence of relatively high values of θ_{el} near $\mathbf{x}_{cl}$ (see Fig. 10c). Of equal importance, the lower-to-middle tropospheric RH fails to exceed 70% in the uptilt semicircle of the inner core, and is lower than 60% near $\mathbf{x}_{cl}$ (Fig. 10b). Whether the foregoing convection-limiting RH deficiency results more from the influx of dry environmental air (midlevel ventilation) or the subsidence of middle tropospheric air originating from the more humid downtilt sector of the tropical cyclone (S22) has not been determined for this particular system.

Once the transition to faster spinup officially begins upon a substantial reduction of the tilt magnitude, LCAPE and RH can be seen to have grown throughout previously deficient regions of the inner core (Figs. 10d and 10e). Figure 10f suggests that a boost of moist entropy in the

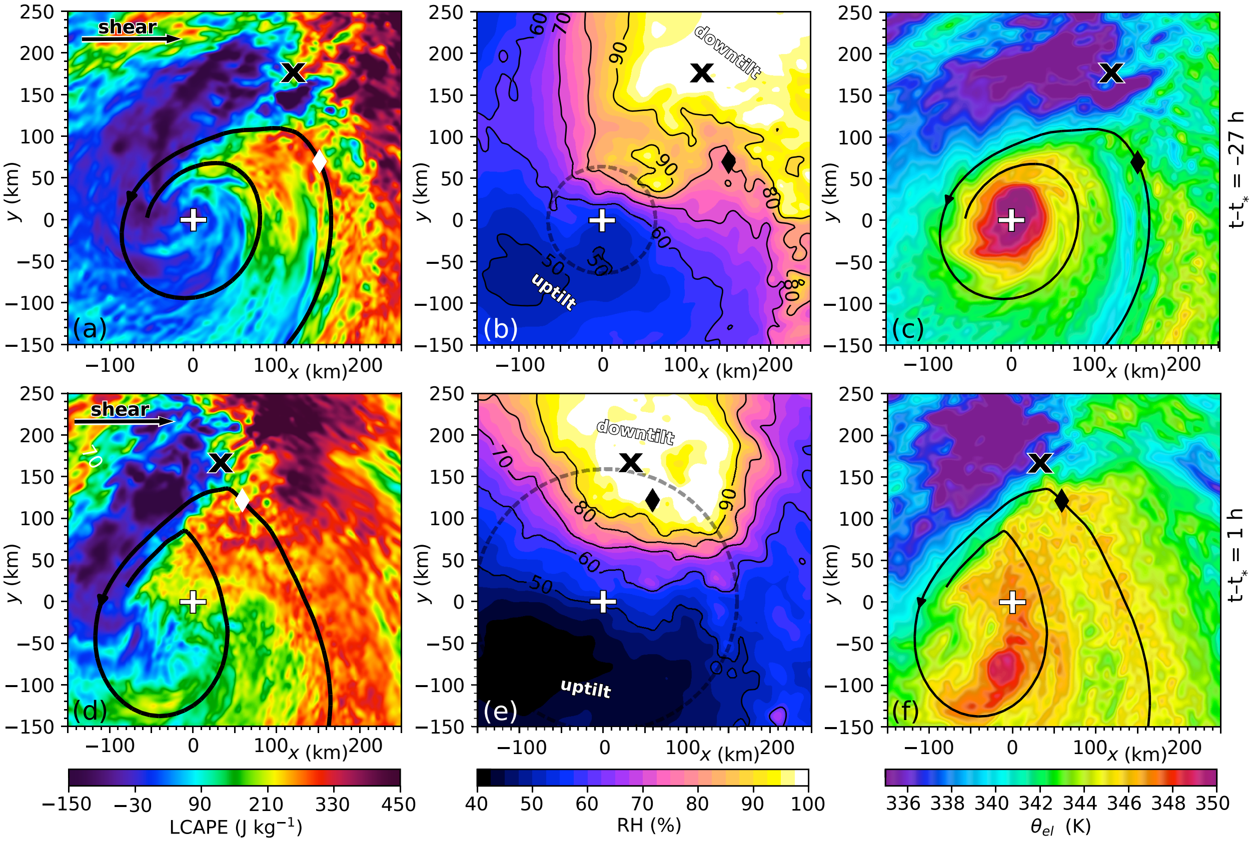

FIG. 11: Distributions of (a,d) LCAPE, (b,e) lower-to-middle tropospheric RH and (c,f) boundary layer equivalent potential temperature θ_{el} in a tropical cyclone (top row) 27 h before a type A transition begins $[(t-t_*)/\tau_e = -0.53]$ and (bottom row) 1 h afterward $[(t-t_*)/\tau_e = 0.02]$. Plotting conventions are as in Fig. 10, with the exception of minor changes to the RH and θ_{el} color scales.

boundary layer contributes to the growth of LCAPE. A fuller account of how the enhancements of both LCAPE and RH arise will be given shortly in a broader context. One might reasonably hypothesize that these enhancements facilitate a more symmetric distribution of convection that can readily move inward. In other words, the spread of favorable conditions for convection throughout the central disc of radius r_m would seem to enable the initiation of the ensuing quasi-symmetric mode of intensification that entails early contraction of the inner core.

Figure 11 shows 2-h averages of LCAPE, lower-to-middle tropospheric RH and θ_{el} centered 27 h before and 1 h after the start-time t_* of a type A transition; the simulation corresponds to that in Fig. 4. The pretransitional moist-thermodynamic conditions (top row) are qualitatively similar to those existing before a type S event, but the transitional conditions (bottom row) differ from their type S counterparts owing largely to much greater misalignment of the low-level and midlevel circulations. In contrast to how a tropical cyclone changes heading into a type S transition, here the RH ultimately decreases in the uptilt semicircle of the inner core. The inner-core LCAPE becomes moderately enhanced in the immediate vicinity of the low-level vortex center and to the right of the tilt vector, but not to the left. The transitional deficiency of LCAPE to the left of the tilt vector is similar to that seen one day earlier in conjunction with a low-entropy air stream in the boundary layer that originates on the downwind side of the downtilt convection zone. Focusing within 35 km of the moving convergence center marked by the diamond, one finds a substantial jump in the mean lower-to-middle tropospheric RH from 84 to 97 percent between the pretransitional (Fig. 11b) and transitional (Fig. 11e) snapshots. By contrast, only a minor uptick of LCAPE (from 248 to 255 J kg^{-1}) is seen near the convergence center over the same time period (Fig. 11a to 11d). One might hypothesize that the aforementioned enhancement of RH allows the vertical mass flux and rainfall rate near $\mathbf{x}_\sigma$ to amplify during the type A transition at hand, and during others of its kind (Figs. 9c and 9f). However, the generality of a major pretransitional change of relative humidity within the convergence zone will be challenged below.

3g.2 Group Comparison

The following presents composite analyses of selected moist-thermodynamic fields in tropical cyclones that experience type S or A transitions to fast spinup. A discussion of field averages within the $\mathbf{x}_{cl}$-centered inner core of the tropical cyclone is followed by a discussion of field averages in the vicinity of the low-level convergence center $\mathbf{x}_\sigma$.

Figures 12a and 12b respectively show time series of the lower-to-middle tropospheric RH (defined as in Figs. 10 and 11) and LCAPE averaged within a radius r_m of the low-level vortex center $\mathbf{x}_{cl}$ for systems that experience type S (red) and type A (blue) transitions to fast spinup. As in previous plots, solid dark curves represent group means and the semi-transparent background shading extends from the 20$^{\text{th}}$ to 80$^{\text{th}}$ percentile of the plotted variable. Averages over the entire inner core such as those considered here will be denoted by the subscript "ic" from this point forward.

In agreement with the first example considered above (Fig. 10), the two figures at hand (12a and 12b) show that type S transitions generally coincide with peaks of RH_{ic} and LCAPE_{ic} that follow pronounced troughs. By contrast, type A transitions are seen to typically begin while RH_{ic} and LCAPE_{ic} are depressed (as in Fig. 11). Although LCAPE_{ic} does not appreciably grow after a type A transition, RH_{ic} generally exhibits a prominent post-transitional peak. Such mean

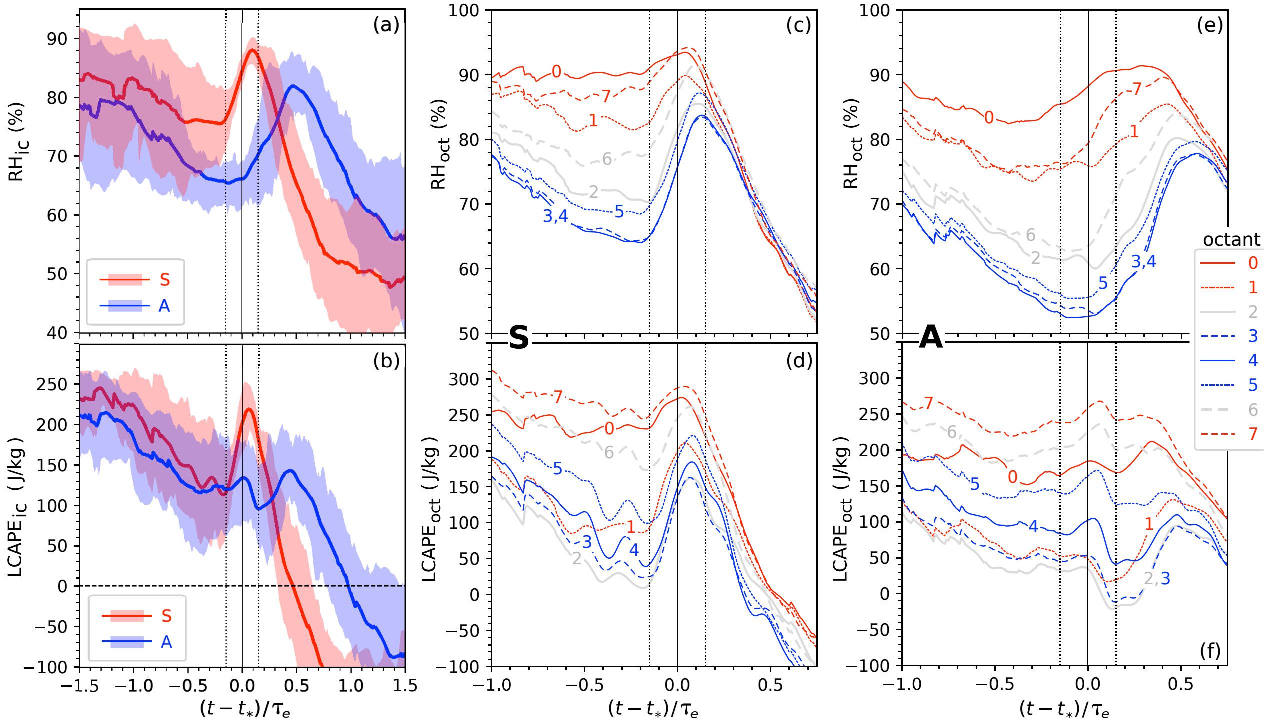

FIG. 12: (a,b) Time series of (a) lower-to-middle tropospheric RH and (b) LCAPE averaged over the entire inner core region of the low-level vortex. Plotting conventions are as in Fig. 5. (c,d) Time series of (c) lower-to-middle tropospheric RH and (d) LCAPE averaged within each inner-core octant [oct ∈ {0, 1,. . . 7}] for systems that undergo type S transitions. Each curve represents the mean for all such systems. The octants are shown in Fig. 13. (e,f) As in (c,d) but for systems that undergo type A transitions.

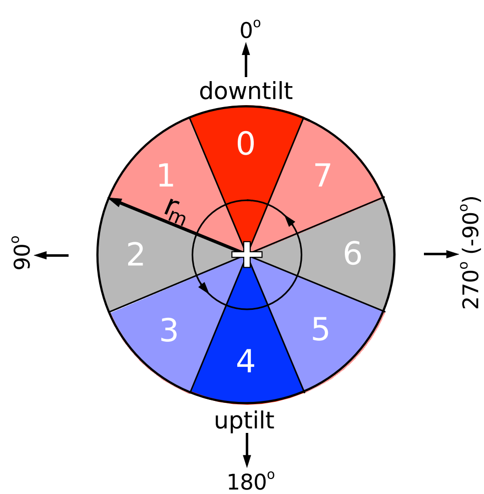

FIG. 13: Division of the inner core of the low-level vortex into octants labeled 0-7. Each octant extends to a radius r_m from the vortex center (+). Notably, octant 0 is centered directly downtilt at 0^o, whereas octant 4 is centered directly uptilt at 180^o. The arrows on the thin central circle convey the approximate direction of the cyclonic surface winds.

environment	trans. type	N_*, N_Δ	$\mathrm{RH}^*_{\mathrm{ic}}$ (%)	$\mathrm{LCAPE}^*_{\mathrm{ic}}$ (J kg^{-1})	$\Delta\mathrm{RH}_{\mathrm{ic}}$ (%)	$\Delta\mathrm{LCAPE}_{\mathrm{ic}}$ (J kg^{-1})
cool SST	S	5, 5	87.7 ± 2.2	177.0 ± 29.4	14.8 ± 8.6	76.3 ± 73.2
	A	12, 10	68.2 ± 5.8	115.2 ± 49.3	0.7 ± 8.3	10.1 ± 64.9
mod SST	S	16, 16	87.3 ± 1.9	213.2 ± 27.7	15.5 ± 8.4	107.3 ± 60.8
	A	19, 14	66.3 ± 7.3	119.4 ± 63.1	-0.6 ± 5.2	20.9 ± 47.4
mod SST, low shear	S	8, 8	86.6 ± 1.2	213.0 ± 22.8	14.4 ± 9.2	105.2 ± 67.1
	A	6, 1	69.1 ± 9.3	147.7 ± 67.1	-2.1	8.8
mod SST, high shear	S	8, 8	88.0 ± 2.2	213.3 ± 31.9	16.6 ± 7.3	109.4 ± 53.8
	A	13, 13	64.9 ± 5.7	106.3 ± 56.6	-0.5 ± 5.4	21.8 ± 49.0
warm SST	S	12, 12	86.9 ± 2.9	231.6 ± 42.4	6.2 ± 7.8	44.7 ± 52.4
	A	10, 7	68.8 ± 4.4	135.9 ± 49.2	3.8 ± 2.6	-28.3 ± 61.6

TABLE 2. Environmental variation of inner-core thermodynamic statistics associated with type S and type A transitions, each expressed as the mean ± 1 standard deviation for a given simulation group. The third column from the left gives the sample sizes for the transitional values (N_*) and pretransitional changes (N_Δ) of $\mathrm{RH}_{\mathrm{ic}}$ and $\mathrm{LCAPE}_{\mathrm{ic}}$; N_Δ can be smaller than N_* owing to the exclusion of systems with a change of environment (ramp-down of u_s) or a first instance of appreciable tilt ($|\mathbf{x}_{cu} - \mathbf{x}_{cl}| > 50$ km) less than a day in advance of t_*.

humidification of the inner core is apparently a common feature of (as opposed to a trigger for) the fast intensification mechanism that involves progressive vertical alignment of the tropical cyclone and contraction of r_m (Figs. 4 and 6).

Figures 12c and 12d respectively show composite time series of octant-averaged inner-core values of lower-to-middle tropospheric RH and LCAPE in systems that experience type S transitions. Figures 12e and 12f are similar, but for systems that experience type A transitions. Figure 13 diagrammatically defines the octants; the octant number increases in the counterclockwise direction from 0, which corresponds to the octant centered directly downtilt. Figures 12c and 12d verify that the enhancements of $\mathrm{RH}_{\mathrm{ic}}$ and $\mathrm{LCAPE}_{\mathrm{ic}}$ immediately preceding type S transitions largely result from enhancements of RH and LCAPE in the octants completely or partly within the uptilt semicircle (2-6). Figure 12e suggests that while the octants with large azimuthal displacements from the tilt vector (2-6) continually lose RH leading up to type A transitions, the octants along the tilt vector and immediately upwind (0 and 7) start gaining RH prior to t_*. The author speculates that the latter result is at least partly attributable to pretransitional growth of r_m (Figs. 6c,11b,e) expanding the downtilt and upwind octants into regions of the tropical cyclone already possessing enhanced RH.

While informative, Fig. 12 does not reveal how the pretransitional and transitional moist-thermodynamic conditions of the inner core might vary with the environment of the tropical cyclone. Table 2 shows the environmental variations of $\mathrm{RH_{ic}}$ and $\mathrm{LCAPE_{ic}}$ during type S and A transitions to fast spinup. Also shown are the changes of both variables leading up to the transitions. Such changes are defined by $\Delta G \equiv G^* - G^-$, in which the asterisk denotes the transitional value (defined previously) of the generic variable G, and the minus-sign appearing in the superscript denotes the time average of G calculated 24 to 12 hours before t_*. The mean values of $\mathrm{RH^*_{ic}}$ appear to have minimal environmental sensitivity for either type S or A transitions. The mean values of $\mathrm{LCAPE^*_{ic}}$ appear to modestly grow with increasing SST, most notably for type S transitions. One might speculate that such growth contributes to the quicker pace of the quasi-symmetric intensification process that follows a type S transition over a warm ocean (Table 1), but other factors including larger surface enthalpy fluxes (S22) could have greater importance. The minor variation of $\mathrm{LCAPE^*_{ic}}$ from one relatively low value to another would seem to have less potential relevance to the asymmetric intensification process that immediately follows a type A transition. Perhaps the most notable results regarding $\Delta\mathrm{RH_{ic}}$ and $\Delta\mathrm{LCAPE_{ic}}$ can be found in the group of simulations with type S transitions to fast spinup. For this group, the means of both pretransitional changes are considerably smaller at warm SSTs than at cool and moderate SSTs. The following demonstrates that the relatively small pretransitional boosts of $\mathrm{RH_{ic}}$ and $\mathrm{LCAPE_{ic}}$ that occur over warm oceans coincide with a qualitatively distinct change of the inner-core vertical temperature profile leading up to t_*.

Figure 14 shows the changes of the vertical profiles of the absolute temperature (ΔT), the water-vapor mixing ratio (Δq_v) and the relative humidity (ΔRH) prior to type S transitions at a moderate SST (28 ^{o}C) and a warm SST (32 ^{o}C). The results shown correspond to averages within a radius r of 25 km from the low-level vortex center $\mathbf{x}_{cl}$, and within the annulus defined by $25 \le r \le 50$ km. These fixed areas generally cover much of the inner core of a tropical cyclone during the time of fast spinup after a type S transition when r_m contracts (on average) from a radius just outside to well-inside the annulus (Fig. 6c). The results at 28 ^{o}C (32 ^{o}C) are qualitatively similar to those for any cool-to-moderate (warm) SST. In both cases, the day preceding t_* entails deep moistening of the inner core. On the other hand, opposite temperature changes in the lower troposphere above the boundary layer occur at relatively low and high SSTs. The former case

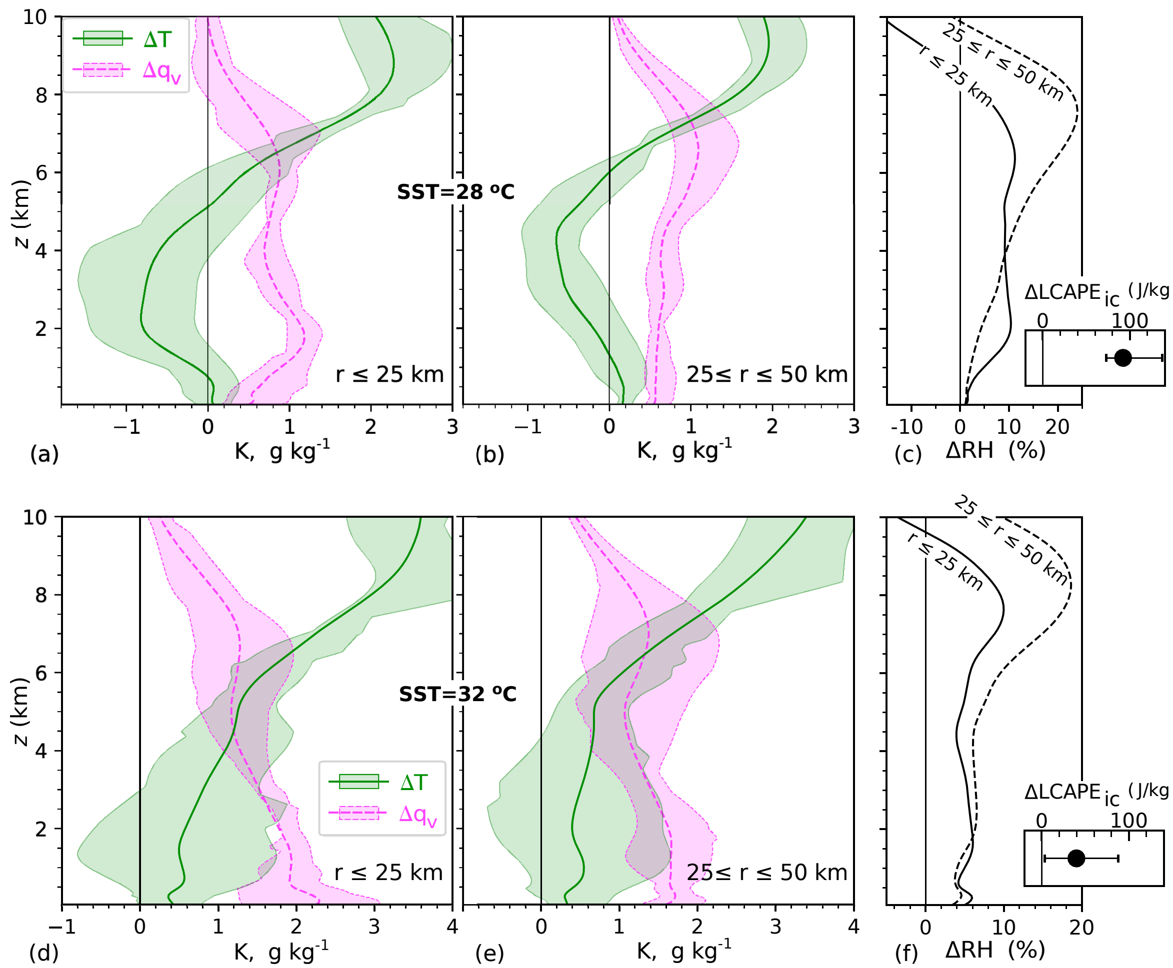

FIG. 14: (a,b) Changes of absolute temperature (ΔT; green) and the water-vapor mixing ratio (Δq_v; purple) during the day leading up to a type S transition at an SST of 28 ^{o}C, averaged over (a) a circular disc of radius $r = 25$ km from the low-level vortex center $\mathbf{x}_{cl}$ and (b) the annulus defined by $25 \le r \le 50$ km. The dark solid or dashed curve represents the z-dependent mean of the plotted variable for all pertinent simulations, whereas the color-matched semi-transparent shading extends horizontally from the z-dependent 20$^{\text{th}}$ to 80$^{\text{th}}$ percentile. (c) Corresponding group-mean changes of relative humidity averaged over the disc of panel-a (solid curve) and annulus of panel-b (dashed curve). The inset shows the group-mean change of LCAPE$_{\text{ic}}$ (circle); the error bars extend from the 20$^{\text{th}}$ to 80$^{\text{th}}$ percentile. (d-f) As in (a-c) but for simulations with an SST of 32 ^{o}C.

shows cooling (Figs. 14a-b), whereas the latter case shows warming (Figs. 14d-e). Whereas the cooling acts to enhance RH and LCAPE, the warming acts to reduce them. Free-tropospheric moistening is apparently sufficient (on average) to counteract the coincident warming and produce a modest positive pretransitional change of RH over warm oceans (Fig. 14f). The combination of moistening and warming of the boundary layer is also sufficient (on average) to account for the modest positive change of LCAPE$_{\text{ic}}$ (inset of Fig. 14f).

The preceding discussion focused on the moist-thermodynamic conditions of the inner core of the tropical cyclone over a relatively short time frame surrounding a transition to fast spinup. Before moving on, it is worthwhile to comment on some additional aspects of the broader time series of $\mathrm{RH_{ic}}$ (Fig. 12a) and $\mathrm{LCAPE_{ic}}$ (Fig. 12b). To begin with, both variables decay following alignment at or after t_* in association with the formation of a relatively warm and dry eye. Moreover, both variables generally exhibit decay trends during the early phase of slow spinup. While these decay trends have not been elucidated through rigorous analysis, one might imagine that the early decline of $\mathrm{RH_{ic}}$ ($\mathrm{LCAPE_{ic}}$) is partly a growing effect of tilt-related midlevel (downdraft) ventilation combined with mesoscale subsidence. From a complementary perspective, one might surmise that the decay trends in any particular system partly result from warming above the surface vortex required to maintain approximate nonlinear balance during slow surface wind speed intensification or increasing μ. It should not go unnoticed that before the two moist-thermodynamic variables under consideration begin to decline $[(t-t_*)/\tau_e < -1]$, their values can be comparable to those found during type S transitions to fast spinup.[6] This suggests that while relatively high values of $\mathrm{RH_{ic}}$ and $\mathrm{LCAPE_{ic}}$ may facilitate a type S transition, they are insufficient to activate a quasi-symmetric mode of fast spinup when substantial kinematic impediments are present or able to promptly develop (see sections 3d-f).

The next issue to be addressed is whether there exists a consistent change in the moist-thermodynamic conditions of the convergence zone that could trigger a type A transition. Figures 15a and 15b respectively show time series of the lower-to-middle tropospheric RH and LCAPE averaged within 35 km of the convergence center $\mathbf{x}_\sigma$. The foregoing average will be denoted by the subscript "cz". Here the group mean of $\mathrm{RH_{cz}}$ is fairly high ($91-96\%$) before and during transitions of either type S or A. The previously seen "major" enhancement of RH above the moving convergence zone leading up to a type A transition (section 3g.1) does not appear to be universal. Although a small change could theoretically cause an instability, the author would be surprised if a modest rise of $\mathrm{RH_{cz}}$ starting from 91% (or so) is necessary for enabling the fast spinup of an asymmetric tropical cyclone.[7] The mean values of $\mathrm{LCAPE_{cz}}$ are also seen to be relatively

[6]For most cases, these values are strongly linked to the state of the tropical cyclone prior to introducing shear at $\tau_\uparrow$. For the complete set of systems that experience type S or A transitions, the 20$^{\text{th}}$ and 80$^{\text{th}}$ percentiles of $(\tau_\uparrow - t_*)/\tau_e$ are -1.8 and -1.1.

[7]A similarly modest rise from roughly 91 to 94 percent is seen when the relative humidity is averaged over a thinner layer with a lower boundary ($1 \leq z \leq 3$ km).

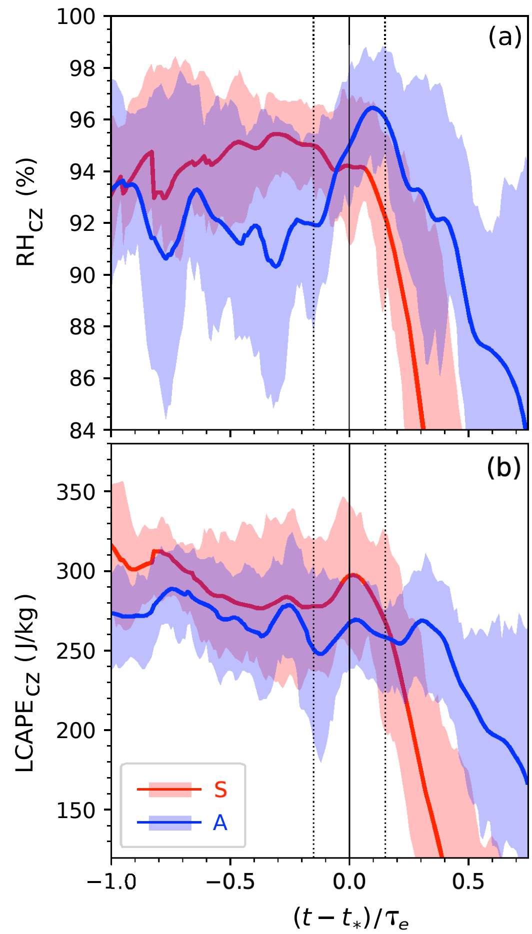

FIG. 15: Time series of (a) lower-to-middle tropospheric RH and (b) LCAPE averaged within 35 km of the convergence center $\mathbf{x}_\sigma$ for type S (red) and A (blue) transitions. Plotting conventions are as in Fig. 5.

high before and during transitions of either type S or A. The slightly negative trend seen before a type A transition (also seen before a type S transition) would seem to disprove any notion that a local boost of LCAPE enables the amplification of convection in the convergence zone during that transition (Figs. 9c and 9f). In summary, the values of $\mathrm{RH_{cz}}$ and $\mathrm{LCAPE_{cz}}$ on average seem to be suitable for the onset of fast spinup any time before a type A (or S) transition actually occurs.

3.h Core Reformation

One of the most dramatic transformational events in a tropical cyclone that can be linked to the onset of fast spinup is core (or center) reformation. As noted in section 1, the process typically involves the rapid emergence of a strong subvortex in the downtilt convection zone that within a few hours dominates the broader parent cyclone and takes over as the inner-core. The question at hand is how transitions via core reformation fit into the quasi binary classification scheme proposed herein. The main issue is whether core reformation occurs before, after or during the transition period. If core reformation were to occur appreciably before t_* and result in permanent alignment, then its function would be to set the stage for a type S transition. If core reformation were to occur appreciably after t_* in a strongly tilted tropical cyclone, then it would be considered a phase of the fast spinup process following a type A transition. If core reformation occurs during the transition period in which μ^* is measured, the objective classification of that transition could be either type A or S (or G) depending on how the ratio of the time-averages of two abruptly changing quantities (the tilt magnitude and r_m) works out. Whether the subsequent intensification mechanism is quasi-symmetric or asymmetric would depend on the extent to which the new core is resilient against vertical wind shear.

Clear-cut permanent core reformation events are not very common in the simulations under consideration, but occasionally take place. One particular event occurring in a system with an SST of 32 ^{o}C and a 0–12 km shear magnitude of 10.5 m s^{-1} will be considered for illustrative purposes. Figure 16a shows the time series of V_m. A prominent spike occurs within the short (6-h) period after t_* during which μ^* is measured. The V_m-spike follows a jump of the official low-level vortex center $\mathbf{x}_{cl}$ away from the center of the weak parent cyclone ($\mathbf{x}_{cl}^b$ defined in appendix B1) to a subvortex intensifying within the downtilt convergence zone (Figs. 16d–e). The jump results in major discontinuous contractions of the tilt magnitude, ℓ and r_m (Fig. 16b) that are only partially reversed as the reconfigured tropical cyclone begins to evolve under the influence of vertical shear (Figs. 16e–f). Remarkably, the dramatic reduction of the tilt magnitude is largely compensated for by the reduction of r_m, so as to keep μ above the threshold ($\mu_o + \delta\mu_o = 0.85$) for a type A transition during almost the entire event (Fig. 16c). The calculated transitional value of μ is given by $\mu^* = 1.15$. Furthermore, the value of μ tends to stay above unity for approximately 20 h after t_* (not completely shown), indicating that the continuation of intensification to that point (Fig. 16a) occurs while the tropical cyclone is asymmetric. To reiterate, this particular variant of a type A transition appears to be uncommon in the data set under consideration; during the 6-h measurement period for such transitions, the tilt magnitude, r_m and ℓ usually stay large (Figs. 6b-c,8c).

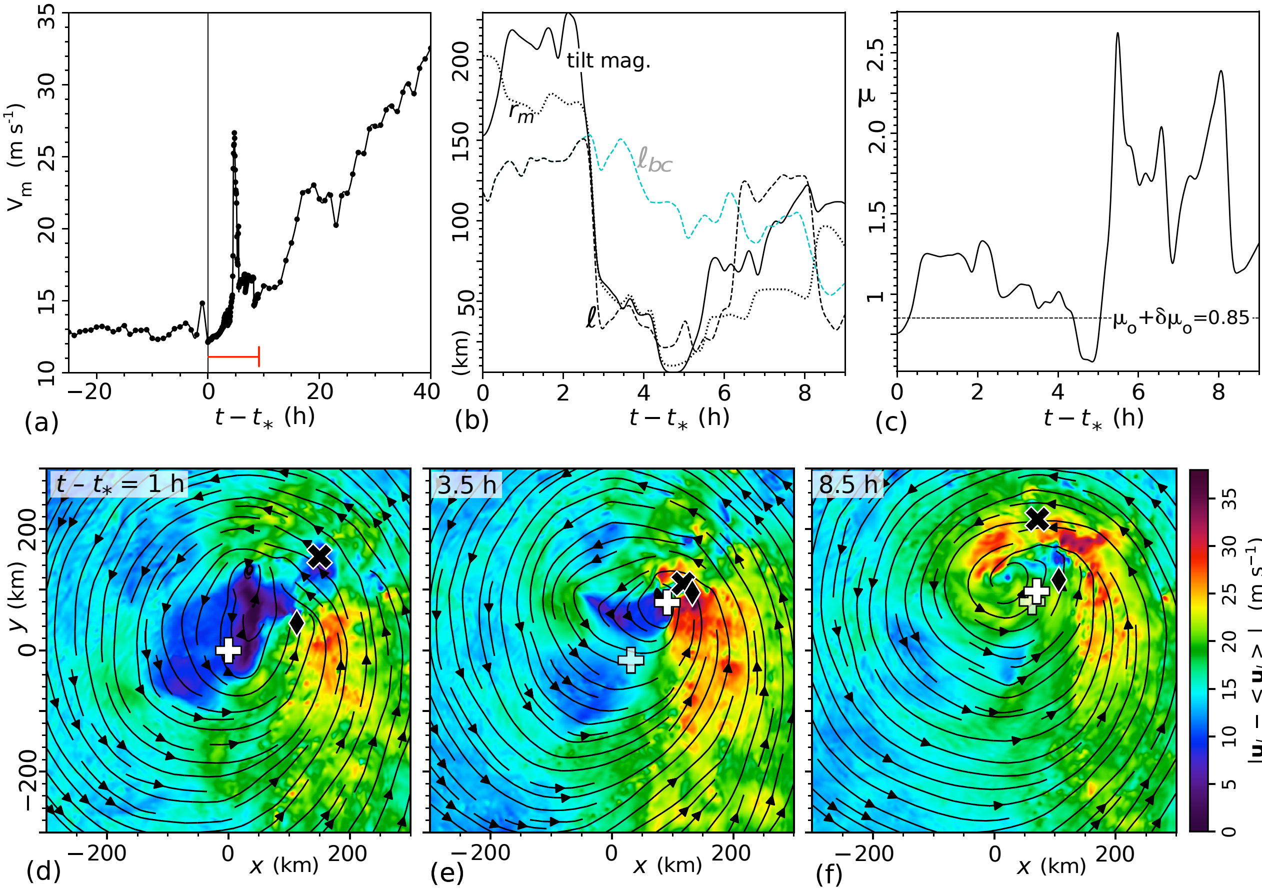

FIG. 16: Special type A transition involving core reformation. (a) Time series of V_m; the spacing between dots (3 min for $0 \leq t - t_* \leq 9$ h and 1 h elsewhere) corresponds to the local sampling interval. (b) Time series of the tilt magnitude (solid), r_m (dotted), $\ell \equiv |\mathbf{x}_\sigma - \mathbf{x}_{cl}|$ (dashed black) and $\ell_{bc} \equiv |\mathbf{x}_\sigma - \mathbf{x}^b_{cl}|$ (dashed light blue) during the first 9 h after t_* [marked by the red bar near the time axis in (a)]. (c) Time series of μ over the same 9 hours. (d-f) Streamlines and magnitude (color) of the horizontal velocity field in the boundary layer $\mathbf{u}_l$ minus its domain average $\langle \mathbf{u}_l \rangle_{xy}$ at (d) $t - t_* = 1$ h, (e) 3.5 h and (f) 8.5 h. The opaque and semi-transparent white plus-signs respectively mark the official low-level vortex center of the tropical cyclone ($\mathbf{x}_{cl}$) and the broad cyclone center ($\mathbf{x}^b_{cl}$); the two centers coincide in (d). The black $\times$ marks the midlevel vortex center ($\mathbf{x}_{cu}$), and the black diamond marks the convergence center $\mathbf{x}_\sigma$. The origin of the coordinate system is fixed relative to the surface of the earth.

4. Discussion

The following discusses how the preceding results relate to earlier observations of transitions to rapid intensification in natural tropical cyclones. One original objective of this modeling study was to search a broad region of parameter space for novel transition types that might have been overlooked owing to observational limitations. In the end, this study may have served more to corroborate earlier observations and to further elucidate the role of tilt in differentiating transition dynamics.

To begin with, there are numerous observations of tropical cyclones experiencing transitions that seem to resemble those of type S. Comprehensive surveys of satellite data have suggested that substantial azimuthal spreading of inner-core precipitation akin to that which occurs upon a type S transition commonly transpires by the initial phase of rapid intensification (e.g. Harnos and Nesbitt 2011,2016c; Kieper and Jiang 2012; Tao et al. 2015,2017; Fischer et al. 2018). There are also observations qualitatively consistent with the characteristic stagnation or decline of the precipitation rate within 100 km of the convergence center prior to a type S transition. Specifically, Tao et al. (2017) reports that inner-core "rainfall intensity and total volumetric rain [typically] do not increase much until several hours after" the onset of rapid intensification.

Of particular relevance to this study, Harnos and Nesbitt (2011) previously presented empirical evidence for (at least) two modes of rapid intensification. The introduction of their 2016b paper concisely summarizes their observational finding as follows:

> Harnos and Nesbitt (2011) used 20+ years of passive microwave ice scattering signals to suggest two shear-delineated structures associated with [tropical cyclones] undergoing [rapid intensification]: widespread modest convection with a relatively symmetric ring-like presence under low wind shear and asymmetric intense convection preferentially downshear and downshear-left under high shear.

The relatively "asymmetric intense convection" of the nominal high-shear mode of rapid intensification seems akin to the relatively high levels of vertical mass-flux and precipitation that are usually found in close proximity to the convergence center during and shortly after a type A transition to fast spinup. A "downshear and downshear-left" preference for convection in the high-shear mode also seems consistent with intensification initiated by a type A transition, at which time the position of the convergence center ($\mathbf{x}_\sigma - \mathbf{x}_{cl}$) has a polar angle of 67 ± 23^o measured cyclonically from the shear-vector.[8] On the other hand, we have seen (Fig. 4c) that the most prominent region of convection can readily migrate into the upshear semicircle ($x - x_{cl} < 0$) during the asymmetric intensification process that follows a type A transition. Perhaps a more important difference be-

[8]This angle is appreciably smaller than the corresponding tilt angle $\varphi^*_{\text{tilt}} = 91 \pm 21^o$ shown for type A transitions in Fig. 7. Schecter (2023) reported analogous anticyclonic displacements of the convective heating center from the midlevel vortex center (as here defined) in cloud resolving simulations of tilted tropical cyclones.

tween the asymmetric modes of fast spinup considered here and those described by Harnos and Nesbitt above could be the extent to which the coinciding environmental wind shear determines the precipitation asymmetry at and shortly after t_*. Appendix C3 demonstrates how the normalized tilt magnitude is a better discriminator of such asymmetry than the coinciding shear magnitude for the simulations at hand.

Of course, Harnos and Nesbitt are neither the first nor the most recent researchers to have presented a binary conceptualization of transitions to fast spinup based completely or partly on observations. Long ago, Holliday and Thompson (1979) suggested that transitions to rapid deepening of the central pressure naturally divide into those preceded by moderate or slow deepening. The extent to which the observed changes from moderate to rapid deepening correspond to transitions of the intensification rate sharp enough for inclusion in the present study is unclear. Nevertheless, the tilt-based classification scheme expounded herein appears to be marginally consistent with that of Holliday and Thompson in that the 24-h intensification rates (for V_m) preceding transitions of type S tend to be larger than those preceding transitions of type A (Table 1; cf. appendix C2).

In connection to both global convection permitting simulations and supportive observational data, Judt et al. (2023) discussed a binary perspective in which transitions lead to either *marathon* or *sprint* modes of rapid intensification. Fundamentally, the marathon mode is “characterized by a moderately paced and long-lived intensification period,” whereas the sprint mode is “characterized by explosive and short-lived intensification bursts.” The marathon mode is described as symmetric in nature, whereas the sprint mode is described as asymmetric. The archetypal transition to a sprint mode illustrated by Judt and coauthors entails core reformation similar to that observed (for instance) by Molinari and Vollaro (2010). As currently seen by the author, the foregoing binary perspective differs from that of the present study. Both composite and individual time series of tropical cyclone intensity (Figs. 5,C1-C2) suggest that transitions of either type S or A commonly initiate long-lived periods of fast spinup similar to those characterizing marathon modes of rapid intensification. Furthermore, core reformation is not essential to type A (or S) transitions.

One might reasonably contend that any binary classification scheme including that proposed herein will paint an incomplete picture of transitions to fast spinup. The clustering of the vast majority of data points into two well-separated groups (Fig. 2) was a convenient result of the present study with questionable relevance to the distribution of natural transitions. The existence of some (type G) transitions outside of the two main clusters hints at a fuzzier reality. Even within a single (type A) cluster we have seen mechanical differences in the transitions [those involving and (normally) not involving core reformation] that encourage the introduction of subcategories. There are also observationally based reasons to believe that additional categories may be needed to adequately classify transitions to fast spinup in systems beyond those (considered herein) with unidirectional environmental vertical wind shear maximized in the middle troposphere. Ryglicki et al. (2018a) for example suggests that there may exist unique aspects to the precursors and manifestations of rapid intensification in tropical cyclones exposed to shallow upper-tropospheric shear layers.

Moving beyond classification issues, it is worth remarking that a variety of observational studies have suggested a connection between substantial intensification and relatively strong contributions to moist convection (latent heat release) at or inside the radius of maximum wind speed (Stevenson et al. 2014; Susca-Lopata et al. 2015; Rogers et al. 2013–16). The analysis of idealized simulations in section 3f did not explicitly examine the distribution of heating relative to the maximum wind speed of the primary circulation at any particular altitude, but did show that the composite mean of ℓ (the distance of the low-level convergence center from $\mathbf{x}_{cl}$) normalized to r_m tends to hover above unity until shortly before a transition (of type S or A) to fast spinup. Such a result was deemed consistent with theory. Here we add that it seems consistent with the aforementioned observed link between robust intensification and pronounced inner (as opposed to outer) convection insofar as the most important convective activity of an asymmetric tropical cyclone occurs near its convergence center.

5. Conclusion

Transitions from slow to fast spinup during tropical cyclone intensification in cloud resolving simulations have been examined over wide ranges of SSTs and environmental vertical wind shears. The transitions have been classified into two types depending on whether they occur when the tropical cyclone is relatively untilted and symmetric (S) or tilted and asymmetric (A). The probability for either type of transition in a given environment has not been determined for a sufficiently broad spectrum of initial conditions, but both appear to be physically possible at any SST between 26 to 32 ^{o}C combined with either weak or moderate vertical wind shear (see Figs. 2 and C3).

The composite analysis presented herein suggests the following scenario surrounding a type S transition. An ordinary type S transition is preceded by gradual declines of the tilt magnitude and the radius of maximum wind speed r_m in the boundary layer. The decay of the tilt magnitude begins to accelerate at about the time $t_\perp$ when the cyclonically rotating tilt vector becomes perpendicular to the direction of the environmental vertical wind shear. Between then and the transition period, the tilt magnitude reduces to less than one-half of r_m. The alignment coincides with pronounced growth of LCAPE and lower-to-middle tropospheric RH in the central and uptilt regions of the inner core of the surface vortex. Such moist-thermodynamic changes may enable the azimuthal spreading of inner-core convection seen during the transition period, and the onset of a quasi-symmetric mode of fast-spinup that initially entails a rapid contraction of r_m.

Tropical cyclones that eventually experience type A transitions tend to acquire larger tilts during their initial developments. The mean transitional values of the tilt magnitude and r_m substantially exceed those found during type S transitions. Moreover, the mean transitional ratio μ of the tilt magnitude to r_m is approximately 1 as opposed to 0.4. Consistent with such major misalignment, type A transitions characteristically occur while convection is still concentrated far downtilt and while the inner-core averages of LCAPE and lower-to-middle tropospheric RH are depressed. Of further note, the azimuthally averaged cyclonic surface winds are generally weaker during type A than during type S transitions.

A composite analysis has shown that the lead-up to a type A transition commonly entails gradual amplifications of the meso-β scale surface precipitation rate P and lower-middle tropospheric vertical mass flux M around the principal low-level convergence center $\mathbf{x}_\sigma$. Similar amplifications are seen before a type S transition, but the type S and A growth trends for either P or M averaged within 100 km or less of $\mathbf{x}_\sigma$ noticeably diverge shortly before the transition time t_*. Whereas the aforementioned averages of P and M drop just before a type S transition alongside the onset of a symmetrization trend, they distinctly grow just before a type A transition to levels not occurring previously (in the mean) for either case. The enhancement of M near $\mathbf{x}_\sigma$ that is linked to a type A transition may well be an important initial ingredient of the asymmetric mode of fast spinup that operates immediately after t_*. Interestingly, only subtle changes of LCAPE and RH in the vicinity of $\mathbf{x}_\sigma$ were found on average to precede or coincide with the local enhancement of M. A more expansive investigation would seem necessary to fully elucidate any moist-thermodynamic changes within a tropical cyclone that may be essential to triggering a type A transition.

That being said, the present study seems to have provided a fairly clear picture of various kinematic changes to the structure of a tropical cyclone that commonly precede type A transitions to fast spinup. To begin with, type A transitions occur on average at the time $t_{\perp}$ when the tilt vector crosses into the upshear semicircle. The coinciding nullification of misalignment-forcing may well facilitate rapid decay of the tilt magnitude, which in concert with quick contractions of r_m and the characteristic precipitation radius r_p appears to be an integral part of the initially asymmetric fast spinup mechanism. Furthermore, type A transitions are commonly preceded by substantial declines of μ to values near 1. Along with the reduction of μ to unity, the center of the convergence zone initially located outside the maximal surface winds becomes situated roughly at r_m. Such a change, which also precedes type S transitions, has the potential to appreciably increase the IR (e.g. Schecter 2020). Another notable kinematic precursor to a type A transition is a reduction of the distance between the convergence center and midlevel vortex center to a magnitude that on average approximately equals the midlevel radius of maximum wind speed. The significance of this change to the vigor of local convection and surface wind speed intensification could be a worthwhile topic of future study.

Section 4 discussed existing observations of transitions to fast spinup in tropical cyclones with either quasi-symmetric or asymmetric distributions of inner-core precipitation. As explained therein, the present study has corroborated many of the observations while providing some additional details on how each type of transition transpires (in the simulations at hand). One distinctive feature of this study has been to expound the central role of tilt— which is not necessarily commensurate with the coinciding environmental vertical wind shear —in differentiating the transition types. This study has also underscored that the initiation of fast spinup in a strongly tilted tropical cyclone with highly asymmetric convection (a type A transition) need not and often does not entail an archetypal core reformation event.

Acknowledgments: The author would like to express his gratitude to three anonymous reviewers for their constructive feedback on the original version of this paper, and to Dr. George Bryan of the National Center for Atmospheric Research (NCAR) for developing and maintaining the atmospheric model used for this study (CM1). The author also thanks student project-participants Ian Mansfield and Brittany Lazzaro for conducting the supplemental simulations (see appendix A) that were incorporated into the composite analyses presented herein. Most of the simulations in the data set used for this study were made possible with resources provided by NCAR's Computational and Information Systems Laboratory (doi:10.5065/D6RX99HX). This work was supported by the National Science Foundation under Grant AGS-2208205.

Data Availability Statement: Namelist files and initial conditions in the form of netCDF CM1-restart files for selected simulations will be available at doi:10.5281/zenodo.10951675 upon acceptance of this manuscript. Archived simulation output files too large and numerous for public repositories will be available to researchers upon request sent to schecter@nwra.com. Modifications to CM1 version 19.5 used to add time-dependent environmental shear flows (section 2a) and peripheral Rayleigh damping with a circular inner boundary (appendix A) are presently available at doi:10.5281/zenodo.7637579.

Appendix A: Simulation Details

Table A1 summarizes the simulations that are used for the present study. The simulations are separated into groups with a specified SST (first column from the left), and into subgroups (second and third columns) determined by the initial vortex structure (PD or MR) and the τ-couplet specifying when the environmental shear flow is ramped up ($\tau_\uparrow$) and down ($\tau_\downarrow$). The fourth column lists the kinds of shear layers found in each subgroup, with L1 corresponding to $(z_\alpha, \delta z_\alpha) = (5.0, 2.5)$ km and L2 corresponding to $(z_\alpha, \delta z_\alpha) = (5.5, 3.5)$ km. The fifth column shows the range of the shear strength parameter $2U_s' \equiv 2U_s \Upsilon$ before the reduction period (implicitly after ramp-up) and after the reduction period in each subgroup. The two right-most columns show the total number of simulations conducted in each subgroup (N) and the number of transitions from slow to fast spinup found to occur in that subgroup (N_t).[9] The sums of N and N_t are also displayed for each SST. Readers may consult appendix C3 (Fig. C3) for a depiction of how various types of transitions are spread over the environmental parameter space of the simulations.

The simulations with $\tau_\uparrow > 0$ in Table A1 were originally conducted for the present study, whereas those with $\tau_\uparrow = 0$ were pulled in from a separate study to moderately increase the amount of data. Hereafter, the former (latter) will be called the main (supplemental) simulations. The main simulations were run with version 19.5 of CM1 tailored to include time-dependent environmental shear flows and Rayleigh damping near the periphery of the horizontal domain. The aforemen-

[9]Two transitions (one of type A followed by another of type S) occurred in one particular simulation with an SST of 26 ^{o}C, $2U_s' = 5.0$ m s^{-1} after ramp-up, and $\tau_\downarrow \to \infty$. All other simulations had 1 or 0 transitions. All transitions in simulations with finite $\tau_\downarrow$ occur after $\tau_\downarrow + \delta\tau_\downarrow$. As noted in section 2b, a transition is counted only if it occurs before the tropical cyclone achieves minimal hurricane strength in the azimuthal mean.

SST (^{o}C)	**Initial Vortex**	**Shear Timing** $\tau_\uparrow$, $\tau_\downarrow$ (h)	**Shear Layer**	**Shear Strength** ($2U_s'$; m/s) $t < \tau_\downarrow$, $t \geq \tau_\downarrow + \delta\tau_\downarrow$	N	N_t
26	PD	0, ∞	L2	2.00–6.00, —	5	1
		36, ∞	L1,L2	1.25–5.50, —	8	5
		60, ∞	L1,L2	2.50–7.50, —	11	6
		60, 102	L1	7.50, 0–5.00	2	2
		60, 93	L2	7.50, 0–5.00	3	3
	MR	0, ∞	L2	4.00, —	1	0
					sum: 30	sum: 17
27	PD	0, ∞	L2	4.00, —	1	1
28	PD	0, ∞	L2	6.00, —	1	1
		54, ∞	L1,L2	2.50–8.75, —	17	12
		54, 99	L1	7.50, 0–5.00	3	3
	MR	0, ∞	L2	4.00, —	1	0
					sum: 22	sum: 16
29	PD	0, ∞	L2	3.00–8.00, —	4	3
	MR	0, ∞	L2	6.00–8.00, —	2	2
					sum: 6	sum: 5
30	PD	0, ∞	L2	8.00, —	1	1
		48, ∞	L1,L2	2.50–10.00, —	15	12
		48, 90	L1,L2	7.50, 0–5.00	6	6
					sum: 22	sum: 19
31	PD	0, ∞	L2	8.00, —	1	1
	MR	0, ∞	L2	8.00, —	1	1
					sum: 2	sum: 2
32	PD	0, ∞	L2	4.00–10.00, —	5	4
		42, ∞	L1,L2	2.50–11.25, —	14	13
		42, 87	L1,L2	10.00, 0–7.50	5	5
	MR	0, ∞	L2	6.00–10.00, —	2	1
					sum: 26	sum: 23

TABLE A1. Summary of the computational data set excluding the zero-shear simulations used to estimate the maximum potential intensities of the tropical cyclones (appendix B3).

tioned Rayleigh damping entails adding a term of the form $\mathbf{F}_d \equiv -(\mathbf{u} - u_s\hat{\mathbf{x}})\Upsilon_d(r; r_d, \delta r_d)/\tau_d$ to the right-hand side of the tendency equation for the horizontal velocity field $\mathbf{u}$. The dependence of the damping on radius r from the domain center is given by $\Upsilon_d = 0$ for $r \leq r_d$, and $\Upsilon_d = \{1 - \cos[\pi \min(r - r_d, \delta r_d)/\delta r_d]\}/2$ for $r > r_d$. In all of the main simulations, $r_d = 1230$ km, $\delta r_d = 100$ km, and $\tau_d = 300$ s.

The supplemental simulations were conducted with version 21.0 of CM1, modified slightly to handle PD vortex initializations. No supplemental simulation includes peripheral Rayleigh damping. All supplemental simulations incorporate their time-independent shear flows through a standard CM1 configuration procedure. The supplemental simulations also differ from the main simulations in having 50 as opposed to 40 vertical levels.

A small number of simulations failed to complete before the edge of the core of the tropical cyclone neared the edge of the central square (with 2.5-km resolution) of the computational grid.[10] In these cases, the simulations were paused and then resumed with all 2D and 3D fields in the CM1 restart file horizontally shifted so as to allow the tropical cyclone to continue its evolution without a loss of inner resolution.

Appendix B: Analysis Details

B.1 Vortex and Convergence Centers

For the present study, the vortex center in a given layer of the tropical cyclone is computed as in Schecter (2023). Let $\mathbf{u}_\kappa$ denote the vertical average of the horizontal velocity field over the depth of layer κ. Let $\bar{v}_{\kappa,m}$ denote the largest value of the azimuthally averaged tangential component of $\mathbf{u}_\kappa$ $[\bar{v}_\kappa(r)]$ in a polar coordinate system centered at an arbitrary horizontal grid point. The vortex center $\mathbf{x}_{c\kappa}$ corresponds to the special grid point for which $\bar{v}_{\kappa,m}$ is maximal. Unless stated otherwise, the evaluation of $\bar{v}_{\kappa,m}$ ignores the velocity field for $r < r_o = 10$ km. As such, the search for the vortex center ignores potentially intense but generally transient small-scale subvortices.

The variable $\mathbf{x}_{cl}$ appearing throughout the main text is the vortex center in a roughly 1-km deep boundary layer adjacent to the sea surface. The variable $\mathbf{x}_{cu}$ is the vortex center in a roughly 1-km deep atmospheric layer with a mean height of approximately 8 km. The calculation of the broad cyclone center $\mathbf{x}_{cl}^b$ of section 3h is similar to the calculation of $\mathbf{x}_{cl}$, but with $r_o \to 120$ km so as to ignore circulations smaller than those at the upper end of the meso-β scale parameter regime.

In analogy to the vortex center, the convergence center $\mathbf{x}_\sigma$ appearing in the main text corresponds to the origin of the particular polar coordinate system that maximizes $-\bar{u}_{l,m}$. Here, $\bar{u}_{l,m}$ is the largest negative value of the azimuthally averaged radial velocity field (for $r \geq r_o$) in the 1-km deep boundary layer. A moderately large value of r_o (30 km) is used to help reduce undesirable fluctuations in the trajectory of $\mathbf{x}_\sigma$.

[10] All but one of these simulations were from the supplemental set.

B.2 Ad Hoc Objective Algorithm for Identifying Substantial Transitions

The identification of a substantial transition to relatively fast spinup is a multistep process. Step 1 involves converting dV_m/dt into a 7-h running average (IR_a) and finding all local maxima of the resulting time series. Local maxima with values less than a modest threshold (IR_a^o specified below) are regarded as incidental and excluded from further consideration. Step 2 involves finding the broader time interval of "enhanced" intensification encompassing each retained local maximum of IR_a. This enhanced intensification interval (EII) is the time segment around the local maximum of IR_a during which the value of IR_a exceeds 0.2 times that maximum. EIIs that overlap each other or have endpoints separated by less than a small time increment (δt_{gap}) are combined into a single EII. Step 3 determines whether the start of an EII in the reconfigured set corresponds to the time t_* of a substantial transition to relatively fast spinup. For a substantial transition, the mean IR during a time interval of length $\delta\tau_{\mathrm{lu}}$ leading up to the start of the EII must be less than 0.4 times the mean IR during the EII. Moreover, the change of vortex intensity over the EII must exceed a certain threshold ΔV_m^o.

The previously unspecified parameters of the transition-finding algorithm are given by the following formulas:

$$\begin{aligned} &\Delta V_m^o = 0.15 V_{\max}, && \delta\tau_{\mathrm{lu}} = 0.4\tau_e, \\ &\delta t_{\mathrm{gap}} = 0.2\tau_e, \text{ and} && \mathrm{IR}_a^o = 0.4\min(\mathrm{IR}_a^{\mathrm{gm}}, \mathrm{MPIR}), \end{aligned} \tag{B1}$$

in which $\mathrm{IR}_a^{\mathrm{gm}}$ is the global maximum of IR_a in the simulation at hand. Section 3c provides the definitions of $V_{\max}$, MPIR and τ_e; appendix B3 gives SST-dependent values for each.

B.3 Maximum Potential Intensity Estimates

The present study employs a very basic method to estimate the maximum potential intensity $V_{\max}$ of a simulated tropical cyclone. Among other simplifications, the method implicitly neglects shear-related differences in the temporal evolution (over 10 days or less) of certain environmental parameters (besides the SST) that theoretically influence $V_{\max}$, such as the tropopause temperature and near-surface relative humidity (Emanuel 1986; cf. Emanuel and Rotunno 2011). To begin with, 2–3 tropical cyclone simulations initialized with either PD or MR vortices are run without

SST (^{o}C)	$V_{\max}$ (m/s)	MPIR (m/s h^{-1})	τ_e (h)
26	49.8	0.85	58.7
27	53.8	0.99	54.4
28	57.8	1.14	50.6
29	61.8	1.31	47.3
30	65.8	1.48	44.5
31	69.8	1.67	41.9
32	73.8	1.86	39.6

TABLE B1. Estimates of $V_{\max}$ and related parameters.

environmental shear flows at each SST. In each case, the simulation lasts well beyond the time t_γ of maximum tropical cyclone intensity. Let V_{ma} denote the average of V_m (defined in section 2b) during the 24 hours immediately after t_γ. Let $V'_{\max}$ denote the maximum of V_{ma} found at a given SST. A linear regression for $V'_{\max}$ against the SST (K) gives the following working formula for the maximum potential intensity: $V_{\max} \equiv a + b(\mathrm{SST} - 273.15)$, in which $a = -54.23$ m s^{-1} and $b = 4.00$ m s^{-1}K^{-1}. A Pearson correlation coefficient of 0.994 indicates a very good fit. Table B1 lists the values of $V_{\max}$, the MPIR [Eq. (5)] and $\tau_e \equiv V_{\max}/\mathrm{MPIR}$ for all SSTs.

B.4 Precipitation Rate Scaling Factor

The scaling factor for the 2-h surface precipitation rate P in Fig. 9 is given by the following formula: $\xi \equiv \langle \mathcal{P}_R \rangle^{fit}_{32\mathrm{C}} / \langle \mathcal{P}_R \rangle^{fit}_{\mathrm{SST}}$. Here, $\mathcal{P}_R$ is the spatio-temporal average of P within a radius R of the convergence center $\mathbf{x}_\sigma$ as V_m intensifies from 10 to 32.5 m s^{-1}, and $\langle \mathcal{P}_R \rangle_{\mathrm{SST}}$ is the average of $\mathcal{P}_R$ over all simulations with a given SST. The superscript *fit* indicates that the values of $\langle \mathcal{P}_R \rangle_{\mathrm{SST}}$ used to calculate ξ are obtained from a linear regression of the form $\langle \mathcal{P}_R \rangle^{fit}_{\mathrm{SST}} = a + b \times \mathrm{SST}$. With values of $\langle \mathcal{P}_R \rangle_{\mathrm{SST}}$ in cm h^{-1} and SST in ^{o}C, the fit parameters are given by $(a,b) = (-2.262, 0.122)$ for $R = 35$ km, $(a,b) = (-1.628, 0.083)$ for $R = 100$ km, and $(a,b) = (-0.922, 0.043)$ for $R = 200$ km. The Pearson correlation coefficients associated with the regressions vary between 0.86 and 0.88. The scaling factors used for Figs. 9a, 9b and 9c respectively correspond to ξ calculated with $R = 200$, 100 and 35 km.

Appendix C: Supplemental Findings

C.1 Precipitation versus Updraft Asymmetry

Let $G(r', \varphi', t)$ denote a generic field whose spatial dependence is expressed as a function of the radius r' and azimuth φ' of a polar coordinate system centered on $\mathbf{x}_{cl}$. The fractional integral of G over a quadrant of a circular disc of radius d is given by

$$G_\varphi(t;d) \equiv \int_{\varphi-\pi/4}^{\varphi+\pi/4} d\varphi' \int_0^d dr' r' G \Bigg/ \int_0^{2\pi} d\varphi' \int_0^d dr' r' G \,, \tag{C1}$$

in which φ is the central azimuth of the quadrant. Following S22, the quadrantal asymmetry of G is defined by

$$G_{\mathrm{asym}}(t;d) \equiv \sqrt{\frac{4}{3}\sum_\varphi \left[G_\varphi(t;d) - \frac{1}{4}\right]^2}, \tag{C2}$$

in which $\varphi - \varphi_o \in \{0, \pi/2, \pi, 3\pi/2\}$ and φ_o is chosen to maximize the sum over φ. The precipitation asymmetry P_{asym} is obtained by letting G equal the 2-h surface precipitation rate P and (as noted in section 3a) by letting $d = 1.2r_m$.

Alternatively, one might consider the updraft asymmetry $\mathrm{UD}_{\mathrm{asym}}$ given by the right-hand side of Eq. (C2) with d as before and $G \rightarrow \rho w\, H(\rho w - M_o)$ evaluated at a specific height z. Here, ρ is density, w is vertical velocity and M_o is a selected value of ρw above (below) which the Heaviside step-function H is 1 (0). Letting $z = 3.6$ km and $M_o = 1$ kg m^{-2}s^{-1} for illustrative purposes, the mean updraft asymmetry ± 1 standard deviation is given by $\mathrm{UD}^*_{\mathrm{asym}} = 0.60 \pm 0.10$ (0.88 ± 0.07) during transitions of type S (A). Both means of the updraft asymmetry measurably exceed those of P^*_{asym} (section 3a), but transitions of type S consistently have smaller values of $\mathrm{UD}^*_{\mathrm{asym}}$ than transitions of type A. The 1-day pretransitional change of the updraft asymmetry defined as in section 3g.2 is given by $\Delta\mathrm{UD}_{\mathrm{asym}} = -0.21 \pm 0.15$ (-0.01 ± 0.09) for transitions of type S (A), consistent with the pretransitional drop (stagnation) of P_{asym} in Fig. 8a. Qualitatively similar results have been verified when $\mathrm{UD}_{\mathrm{asym}}$ is calculated at 8 km above sea level with $M_o = 0.7$ kg m^{-2}s^{-1} or when halving M_o.

C.2 V_m versus the Absolute Maximum Surface Wind Speed

The definition of tropical cyclone spinup adopted for this study is the amplification of V_m, which represents the maximum value of the azimuthally averaged tangential velocity 10 m above sea level

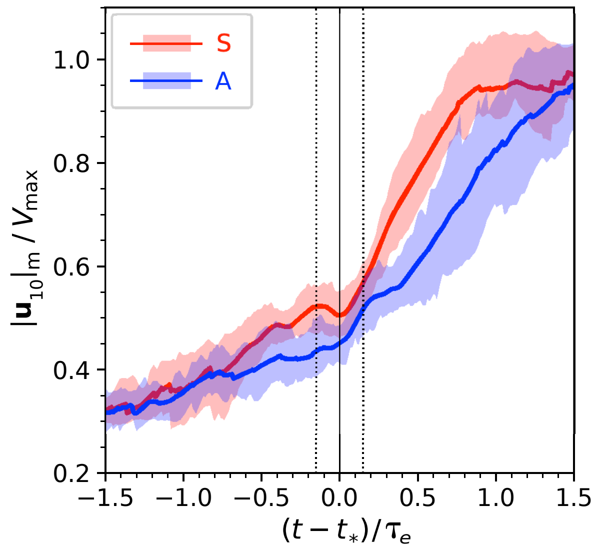

FIG. C1: Time series of the absolute maximum 10-m horizontal wind speed (normalized to V_{max}) in tropical cyclones that experience type S and type A transitions to fast spinup. Plotting conventions are as in Fig. 5.

in a coordinate system centered on $\mathbf{x}_{cl}$. *All conclusions regarding spinup should be viewed in this context.* That being said, one might reasonably ask how the picture of intensification changes upon replacing V_m with the absolute maximum surface wind speed within a tropical cyclone.

Figure C1 shows time series of the instantaneous maximum magnitude of the 10-m ground-relative velocity field ($|\mathbf{u}_{10}|_m$) normalized to V_{max} for tropical cyclones that experience type S and type A transitions. The S-A intensity difference near t_* is diminished upon switching from V_m to $|\mathbf{u}_{10}|_m$ (cf. Fig. 5a), but the acceleration of intensification at this time is basically preserved. Measured immediately before and after t_*, the pretransitional and post-transitional 24-h averages of $\frac{d}{dt}|\mathbf{u}_{10}|_m$ divided by the MPIR respectively equal 0.11 ± 0.14 and 0.54 ± 0.19 for transitions of type S, while equaling 0.14 ± 0.18 and 0.30 ± 0.19 for transitions of type A. For comparison, the pretransitional and post-transitional 24-h averages of $\frac{d}{dt}V_m/\mathrm{MPIR}$ for type S (A) transitions are respectively given by 0.10 ± 0.06 and 0.59 ± 0.15 (0.01 ± 0.08 and 0.35 ± 0.12). Most of the foregoing nondimensional intensification rates are seen to change little when switching from one intensity metric to the other. However, the group-mean 24-h nondimensional intensification rate of $|\mathbf{u}_{10}|_m$ prior to a type A transition (0.14) is an order of magnitude larger than that of V_m (0.01). Of further note, the group-mean nondimensional intensification rate of $|\mathbf{u}_{10}|_m$ during the first 6 h after the initiation of a type A transition (at t_*) is 1.5 times that of V_m.

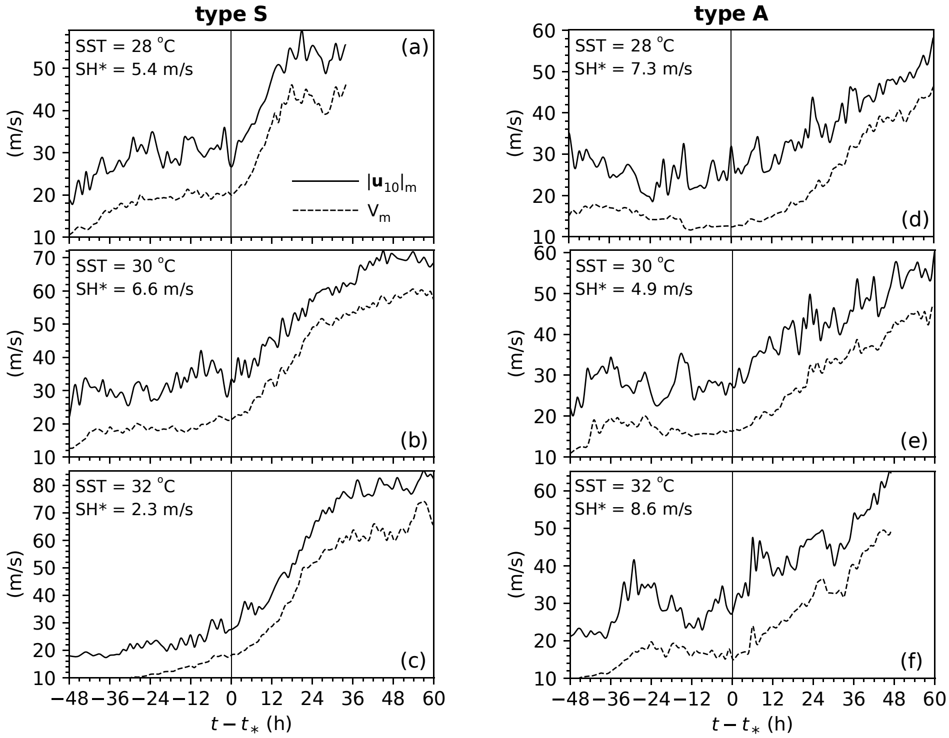

FIG. C2: (a-c) Time series of the absolute maximum 10-m horizontal wind speed (solid) and V_m (dashed) in 3 selected tropical cyclones that experience type S transitions to fast spinup at t_* (thin vertical line). The SST and the 0-12 km environmental vertical wind shear existing at and after t_* (denoted SH*) are printed on the top-left corner of each plot. (d-f) As in (a-c) but for 3 selected tropical cyclones that experience type A transitions. The time series in (a) and (d) respectively correspond to the systems depicted in Figs. 3 and 4.

Figure C2 complements the composite time series (Figs. 5a and C1) by showing V_m and $|\mathbf{u}_{10}|_m$ for 6 selected tropical cyclones that transition to both symmetric and (initially) asymmetric modes of fast spinup. The $|\mathbf{u}_{10}|_m$ curves expectedly have positive displacements and larger fluctuations. For two of the tropical cyclones that experience type A transitions (Figs. C2d and C2f), $|\mathbf{u}_{10}|_m$ appears to begin relatively fast intensification modestly ahead of V_m. On the other hand, $|\mathbf{u}_{10}|_m$ generally follows the smoother and long-lasting post-transitional intensification trend of V_m.

C.3 Relationship Between the Transitional Asymmetry of a Tropical Cyclone and the Coinciding Vertical Wind Shear

Section 4 asserted that for the simulations at hand, the precipitation asymmetry is better correlated to the normalized tilt magnitude μ^* than to the coinciding magnitude of the (0-12 km) environmental vertical wind shear SH* during transitions to fast spinup. This claim is quantitatively supported by the fact that the Pearson correlation coefficient for P^*_{asym} and μ^* is 0.87, whereas that for P^*_{asym} and

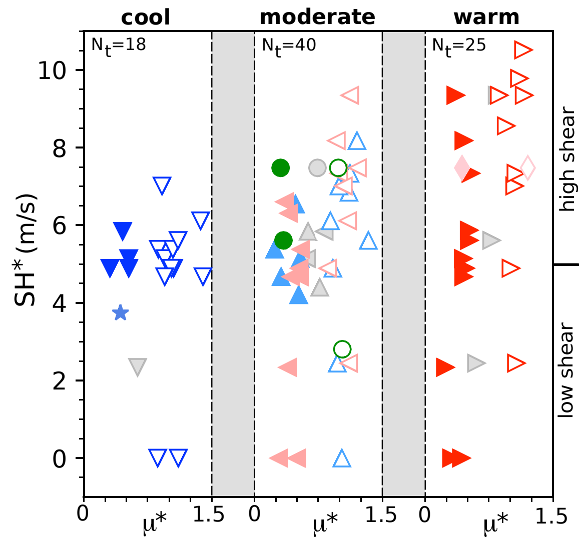

Fig. C3: Locations of type S (color-filled), type A (empty) and type G (gray-filled) transitions to fast spinup in the environmental parameter space defined by SH* and the SST trichotomized into relatively cool (26-27 ^{o}C), moderate (28-30 ^{o}C) and warm (31-32 ^{o}C) values. The horizontal distance between each datum and the left-side of its SST block is proportional to μ^* so as to segregate type S (left) and type A (right) transitions. The upper-left corner of each block shows the total number of transitions (N_t) in the corresponding SST group; the numbers of type S (A) are 5 (12) in the cool group, 16 (19) in the moderate group, and 12 (10) in the warm group. The right-axis shows the dividing line between "low shear" and "high shear" data used for Tables 1 and 2 of the main text. Symbol colors and shapes (but not sizes) are as in Fig. 2.

SH* is merely 0.20. When restricting the calculation to systems in a single SST-group among the triad defined in section 3c, the Pearson correlation coefficient for $P^*_{\rm asym}$ and SH* has a larger but still modest maximum of 0.53 over warm oceans and a minimum of -0.08 over cool oceans.

Figure C3 shows how type S, type A and a small number of type G transitions are distributed over SH* for systems with different SSTs. Consistent with the preceding discussion, the data points for type S and type A transitions are not well-segregated into opposite shear regimes over cool, moderate or warm oceans. On the other hand, only type A transitions can be seen at the very highest shear levels for any SST. Such a result tenuously hints that the SST-dependent upper shear limit for quasi-symmetric (type S) transitions could be smaller than that for asymmetric (type A) transitions.

It is worth noting that there are no simulations in which the shear magnitude changes to SH* an instant before the transition to fast spinup. The shear magnitudes often settle on SH* immediately after $\tau_\uparrow$, and never settle on SH* later than 26 h (10 h) before a transition of type S (A). Only 3 systems with type A transitions obtain their transitional shear magnitudes less than 12 h prior to t_*.

References

Alland, J.J., B.H. Tang, K.L. Corbosiero, and G.H. Bryan, 2021a: Combined effects of midlevel dry air and vertical wind shear on tropical cyclone development. Part I: Downdraft ventilation. *J. Atmos. Sci.*, **78**, 763-782.

Alland, J.J., B.H. Tang, K.L. Corbosiero, and G.H. Bryan, 2021b: Combined effects of midlevel dry air and vertical wind shear on tropical cyclone development. Part II: Radial ventilation. *J. Atmos. Sci.*, **78**, 783-796.

Alvey III, G.R., E. Zipser, and J. Zawislak, 2020: How does Hurricane Edouard (2014) evolve toward symmetry before rapid intensification? A high-resolution ensemble study. *J. Atmos. Sci.*, **77**, 1329-1351.

Alvey III, G.R., M. Fischer, P. Reasor, J. Zawislak, and R. Rogers, 2022: Observed processes underlying the favorable vortex repositioning early in the development of Hurricane Dorian (2019). *Mon. Wea. Rev.*, **150**, 193-213.

Alvey III, G.R. and A. Hazelton, 2022: How do weak, misaligned tropical cyclones evolve toward alignment? A multi-case study using the Hurricane Analysis and Forecast System. *J. Geophys. Res.: Atmospheres*, **127**, e2022JD037268:1-27.

Bryan, G.H., and J.M. Fritsch, 2002: A benchmark simulation for moist nonhydrostatic numerical models. *J. Atmos. Sci.*, **130**, 2917-2928.

Bryan, G. and R. Rotunno, 2009: The maximum intensity of tropical cyclones in axisymmetric numerical model simulations. *Mon, Wea. Rev.*, **137**, 1770-1789.

Brown, R.G., and C. Zhang, 1997: Variability of midtropospheric moisture and its effect on cloud-top height distribution during TOGA COARE. *J. Atmos. Sci.*, **54**, 2760-2774.

Carrasco, C.A., C.W. Landsea, and Y.L. Lin, 2014: The influence of tropical cyclone size on its intensification. *Weather and Forecasting*, **29**, 582-590.

Chou, M.-D., and M. Suarez, 1999. A Solar Radiation Parameterization for Atmospheric Studies. *NASA Tech. Memo.* 104606, **15**, 38 pp.

Chou, M.D., M.J. Suarez, X.Z. Liang, and M.M.H. Yan, 2001: A thermal infrared radiation parameterization for atmospheric studies. *NASA Tech. Memo.* 104606, **19**, 68 pp.

Chen, H., and S.G. Gopalakrishnan, 2015: A study on the asymmetric rapid intensification of Hurricane Earl (2010) using the HWRF system. *J. Atmos. Sci.*, **72**, 531-550.

Chen, X., Y. Wang, J. Fang, and M. Xue, 2018: A numerical study on rapid intensification of Typhoon Vicente (2012) in the South China Sea. Part II: Roles of inner-core processes. *J. Atmos. Sci.*, **75**, 235-255.

Chen, X., J.A. Zhang, and F.D. Marks, 2019. A thermodynamic pathway leading to rapid intensification of tropical cyclones in shear. *Geophys. Res. Lett.*, **46**, 9241-9251.

Chen, X., J.F. Gu, J.A. Zhang, F.D. Marks, R.F. Rogers, and J.J. Cione, 2021: Boundary layer recovery and precipitation symmetrization preceding rapid intensification of tropical cyclones under shear. *J. Atmos. Sci.*, **78**, 1523-1544.

Črnivec, N., R.K. Smith, and G. Kilroy, 2016: Dependence of tropical cyclone intensification rate on sea-surface temperature. *Q. J. R. Meteorol. Soc.*, **142**, 1618-1627.

DeMaria, M., 1996: The effect of vertical shear on tropical cyclone intensity change. *J. Atmos. Sci.*, **53**, 2076-2088.

Dolling, K. and G.M. Barnes, 2012: Warm-core formation in tropical storm Humberto (2001). *Mon. Wea. Rev.*, **140**, 1177-1190.

Donelan, M.A., B.K. Haus, N. Reul, W.J. Plant, M. Stiassnie, H.C. Graber, O.B. Brown, and E.S. Saltzman, 2004: On the limiting aerodynamic roughness of the ocean in very strong winds. *Geophys. Res. Lett.*, **31**, L18306:1-5.

Drennan, W.M., J.A. Zhang, J.R. French, C. McCormick, and P.G. Black, 2007: Turbulent fluxes in the hurricane boundary layer. Part II: Latent heat flux. *J. Atmos. Sci.*, **64**, 1103-1115.

Dunion, J.P., 2011: Rewriting the climatology of the tropical North Atlantic and Caribbean Sea atmosphere. *J. Climate*, **24**, 893-908.

Emanuel, K.A., 1986: An air sea interaction theory for tropical cyclones. Part I: Steady state maintenance. *J. Atmos. Sci.*, **43**, 585-604.

Emanuel, K., 1994. *Atmospheric Convection*, Oxford Univ. Press, New York, 580 pp.

Emanuel, K. and R. Rotunno, 2011: Self-stratification of tropical cyclone outflow. Part I: Implications for storm structure. *J. Atmos. Sci.*, **68**, 2236-2249.

Fairall, C.W., E.F. Bradley, J.E. Hare, A.A. Grachev, and J.B. Edson, 2003: Bulk parameterization of air-sea fluxes: Updates and verification for the COARE algorithm. *J. Climate*, **16**, 571-591.

Finocchio, P.M., S.J. Majumdar, D.S. Nolan, and M. Iskandarani, 2016: Idealized tropical cyclone responses to the height and depth of environmental vertical wind shear. *Mon. Wea. Rev.*, **144**, 2155-2175.

Fischer, M.S., B.H. Tang, K.L. Corbosiero, and C.M. Rozoff, 2018: Normalized convective characteristics of tropical cyclone rapid intensification events in the North Atlantic and eastern North Pacific. *Mon. Wea. Rev.*, **146**, 1133-1155.

Fischer, M.S., P.D. Reasor, B.H. Tang, K.L. Corbosiero, R.D. Torn, and X. Chen, 2023: A tale of two vortex evolutions: Using a high-resolution ensemble to assess the impacts of ventilation on a tropical cyclone rapid intensification event. *Mon. Wea. Rev.*, **151**, 297-320.

Fischer, M.S., R.F. Rogers, P.D. Reasor, and J.P. Dunion, 2024: An observational analysis of the relationship between tropical cyclone vortex tilt, precipitation structure, and intensity change. *Mon. Wea. Rev.*, **152**, 203-225.

Gallina, G., and C. Velden, 2002: Environmental vertical wind shear and tropical cyclone intensity change utilizing enhanced satellite derived wind information. Preprints, *25th Conf. on Hurricanes and Tropical Meteorology*, San Diego, CA, Amer. Meteor. Soc., 3C.5.

Ge, X., T. Li and M. Peng, 2013: Effects of vertical shears and midlevel dry air on tropical cyclone developments. *J. Atmos. Sci.*, **70**, 3859-3875.

Gu, J.F., Z.M. Tan, and X. Qiu, 2019: Intensification variability of tropical cyclones in directional shear flows: Vortex tilt–convection coupling. *J. Atmos. Sci*, **76**, 1827-1844.

Harnos, D.S. and S.W. Nesbitt, 2011: Convective structure in rapidly intensifying tropical cyclones as depicted by passive microwave measurements. *Geophys. Res. Lett.*, **38**, L07805:1-5.

Harnos, D.S. and S.W. Nesbitt, 2016a: Varied pathways for simulated tropical cyclone rapid intensification. Part I: Precipitation and environment. *Q. J. R. Meteorol. Soc.*, **142** , 1816-1831.

Harnos, D.S. and S.W. Nesbitt, 2016b: Varied pathways for simulated tropical cyclone rapid intensification. Part II: Vertical motion and cloud populations. *Q. J. R. Meteorol. Soc.*, **142**, 1832-1846.

Harnos, D.S. and S.W. Nesbitt, 2016c: Passive microwave quantification of tropical cyclone inner-core cloud populations relative to subsequent intensity change. *Mon. Wea. Rev.*, **144**, 4461-4482.

Hendricks, E.A., M.S. Peng, B. Fu, and T. Li, 2010: Quantifying environmental control on tropical cyclone intensity change. *Mon. Wea. Rev.*, **138**, 3243-3271.

Holliday, C.R. and A.H. Thompson, 1979: Climatological characteristics of rapidly intensifying typhoons. *Mon. Wea. Rev.*, **107**,1022-1034.

James, R.P., and P.M. Markowski, 2010: A numerical investigation of the effects of dry air aloft on deep convection. *Mon. Wea. Rev.*, **138**, 140-161.

Jones, S.C., 1995: The evolution of vortices in vertical shear. I: Initially barotropic vortices. *Quart. J. Roy. Meteor. Soc.*, **121**, 821-851.

Judt, F., R. Rios-Berrios, and G.H. Bryan, 2023: Marathon versus sprint: two modes of tropical cyclone rapid intensification in a global convection-permitting simulation. *Mon. Wea. Rev.*, **151**, 2683-2699.

Kaplan, J., and M. DeMaria, 2003: Large-scale characteristics of rapidly intensifying tropical cyclones in the North Atlantic basin. *Weather and Forecasting*, **18**, 1093-1108.

Kaplan, J., M. DeMaria, and J.A. Knaff, 2010: A revised tropical cyclone rapid intensification index for the Atlantic and eastern north Pacific basins. *Weather and Forecasting*, **25**, 220-241.

Kieper, M.E. and H. Jiang, 2012: Predicting tropical cyclone rapid intensification using the 37 GHz ring pattern identified from passive microwave measurements. *Geophys. Res. Lett.*, **39**, L13804:1-7.

Kilroy, G., and R.K. Smith, 2013: A numerical study of rotating convection during tropical cyclogenesis. *Quart. J. Roy. Meteor. Soc.*, **139**, 1255-1269.

Li, Y., Y. Tang, R. Toumi, and S. Wang, 2022: Revisiting the definition of rapid intensification of tropical cyclones by clustering the initial intensity and inner-core size. *J. Geophys. Res.: Atmospheres*, **127**, e2022JD036870:1-12.

Lin, Y., M. Zhao, and M. Zhang, 2015: Tropical cyclone rainfall area controlled by relative sea surface temperature. *Nature Comm.*, **6**, 1-7.

Miyamoto, Y., and D.S. Nolan, 2018: Structural changes preceding rapid intensification in tropical cyclones as shown in a large ensemble of idealized simulations. *J. Atmos. Sci*, **75**, 555-569.

Molinari, J., D. Vollaro, and K.L. Corbosiero, 2004: Tropical cyclone formation in a sheared environment: A case study. *J. Atmos. Sci*, **61**, 2493-2509.

Molinari, J., and D. Vollaro, 2010: Rapid intensification of a sheared tropical storm. *Mon. Wea. Rev.*, **138**, 3869-3885.

Montgomery, M.T., R.K. Smith, 2014: Paradigms for tropical cyclone intensification. *Aust. Meteor. Ocean. Journ.*, **64**, 37-66.

Morrison, H., J.A. Curry, and V.I. Khvorostyanov, 2005: A new double-moment microphysics parameterization for application in cloud and climate models. Part I: Description. *J. Atmos. Sci.*, **62**, 1665-1677.

Morrison, H., G. Thompson, and V. Tatarskii, 2009: Impact of cloud microphysics on the development of trailing stratiform precipitation in a simulated squall line: Comparison of one-and two-moment schemes. *Mon. Wea. Rev.*, **137**, 991-1007.

Munsell, E.B., F. Zhang, J.A. Sippel, S.A. Braun, and Y. Weng, 2017: Dynamics and predictability of the intensification of Hurricane Edouard (2014). *J. Atmos. Sci.*, **74**, 573-595.

Nguyen, L.T., and J. Molinari, 2015: Simulation of the downshear reformation of a tropical cyclone. *J. Atmos. Sci.*, **72**, 4529-4551.

Nguyen, L.T., R.F. Rogers, and P.D. Reasor, 2017: Thermodynamic and kinematic influences on precipitation symmetry in sheared tropical cyclones: Bertha and Cristobal (2014). *Mon. Wea. Rev.*, **145**, 4423-4446.

Nolan, D.S., 2011: Evaluating environmental favorableness for tropical cyclone development with the method of point-downscaling. *J. Adv. Model. Earth Syst.*, **3**, M08001:1-28.

Nolan, D.S., S. Nebylitsa, B.D. McNoldy, and S.J. Majumdar, 2023: Modulation of tropical cyclone rapid intensification by mesoscale asymmetries. *Q. J. R. Meteorol. Soc.*, **150**, 388–415.

Onderlinde, M.J., and D.S. Nolan, 2016: Tropical cyclone-relative environmental helicity and the pathways to intensification in shear. *J. Atmos. Sci.*, **73**, 869-890.

Pendergrass, A.G., and H.E. Willoughby, 2009: Diabatically induced secondary flows in tropical cyclones. Part I: Quasi-steady forcing. *Mon. Wea. Rev.*, **137**, 805-821.

Rappin, E.D., and D.S. Nolan, 2012: The effect of vertical shear orientation on tropical cyclogenesis. *Q. J. R. Meteorol. Soc.*, **138**, 1035-1054.

Reasor, P.D., and M.T. Montgomery, 2001: Three-dimensional alignment and co-rotation of weak, TC-like vortices via linear vortex-Rossby-waves. *J. Atmos. Sci.*, **58**, 2306-2330.

Reasor, P.D., M.T. Montgomery, and L.D. Grasso, 2004: A new look at the problem of tropical cyclones in shear flow: vortex resiliency. *J. Atmos. Sci.*, **61**, 3-22.

Riemer, M., M.T. Montgomery, and M.E. Nicholls, 2010: A new paradigm for intensity modification of tropical cyclones: Thermodynamic impact of vertical wind shear on the inflow layer. *Atmos. Chem. Phys.*, **10**, 3163-3188.

Riemer, M., M.T. Montgomery, and M.E. Nicholls, 2013: Further examination of the thermodynamic modification of the inflow layer of tropical cyclones by vertical wind shear. *Atmos. Chem. Phys.*, **13**, 327-346.

Riemer, M., and F. Laliberté, 2015: Secondary circulation of tropical cyclones in vertical wind shear: Lagrangian diagnostic and pathways of environmental interaction. *J. Atmos. Sci.*, **72**, 3517-3536.

Rios-Berrios, R., C.A. Davis, and R.D. Torn and 2018: A hypothesis for the intensification of tropical cyclones under moderate vertical wind shear. *J. Atmos. Sci.*, **75**, 4149-4173.

Rios-Berrios, R., 2020: Impacts of radiation and cold pools on the intensity and vortex tilt of weak tropical cyclones interacting with vertical wind shear. *J. Atmos. Sci.*, **77**, 669-689.

Rogers, R., P. Reasor, and S. Lorsolo, 2013: Airborne Doppler observations of the inner-core structural differences between intensifying and steady-state tropical cyclones. *Mon. Wea. Rev.*, **141**, 2970-2991.

Rogers, R.F., P.D. Reasor, and J.A. Zhang, 2015: Multiscale structure and evolution of Hurricane Earl (2010) during rapid intensification. *Mon. Wea. Rev.*, **143**, 536-562.

Rogers, R.F., J.A. Zhang, J. Zawislak, H. Jiang, G.R. Alvey, E.J. Zipser, and S.N. Stevenson, 2016: Observations of the structure and evolution of Hurricane Edouard (2014) during intensity change. Part II: Kinematic structure and the distribution of deep convection. *Mon. Wea. Rev.*, **144**, 3355-3376.

Rogers, R.F., P.D. Reasor, J.A. Zawislak, and L.T. Nguyen, 2020: Precipitation processes and vortex alignment during the intensification of a weak tropical cyclone in moderate vertical shear. *Mon. Wea. Rev.*, **148**, 1899-1929.

Ryglicki, D.R., J.H. Cossuth, D. Hodyss, and J.D. Doyle, 2018a: The unexpected rapid intensification of tropical cyclones in moderate vertical wind shear. Part I: Overview and observations. *Mon. Wea. Rev.*, **146**, 3773–3800.

Ryglicki, D.R., Y. Jin, D. Hodyss, and J.H. Cossuth, 2018b: The unexpected rapid intensification of tropical cyclones in moderate vertical wind shear. Part II: Vortex tilt. *Mon. Wea. Rev.*, **146**, 3801–3825.

Schecter, D.A., and M. T. Montgomery, 2003: On the symmetrization rate of an intense geophysical vortex. *Dyn. Atmos. Oceans*, **37**, 55-88.

Schecter, D.A., and M.T. Montgomery, 2007: Waves in a cloudy vortex. *J. Atmos. Sci*, **64**, 314-337.

Schecter, D.A., 2016: Development and nondevelopment of binary mesoscale vortices into tropical cyclones in idealized numerical experiments. *J. Atmos. Sci.*, **73**, 1223-1254.

Schecter, D.A., 2020: Distinct intensification pathways for a shallow-water vortex subjected to asymmetric "diabatic" forcing. *Dyn. Atmos. Oceans*, **91**, 101156:1-25.

Schecter, D.A., and K. Menelaou, 2020: Development of a misaligned tropical cyclone. *J. Atmos. Sci.*, **77**, 79-111.

Schecter, D.A., 2022: Intensification of tilted tropical cyclones over relatively cool and warm oceans in idealized numerical simulations. *J. Atmos. Sci.*, **79** 485-512.

Schecter, D.A., 2023: Intensification rates of tropical cyclone–like vortices in a model with downtilt diabatic forcing and oceanic surface drag. *J. Atmos. Sci.*, **80**, 1787-814.

Stevenson, S.N., K.L. Corbosiero, and J. Molinari, 2014: The convective evolution and rapid intensification of Hurricane Earl (2010). *Mon. Wea. Rev.*, **142**, 4364-4380.

Stone, Ž., G.R. Alvey III, J.P. Dunion, M.S. Fischer, D.J. Raymond, R.F. Rogers, S. Sentić, and J. Zawislak, 2023: Thermodynamic contribution to vortex alignment and rapid intensification of Hurricane Sally (2020). *Mon. Wea. Rev.*, **151**, 931-951.

Susca-Lopata, G., J. Zawislak, E.J. Zipser, and R.F. Rogers, 2015: The role of observed environmental conditions and precipitation evolution in the rapid intensification of Hurricane Earl (2010). *Mon. Wea. Rev.*, **143**, 2207-2223.

Tang, B., and K. Emanuel, 2012: A ventilation index for tropical cyclones. *Bull. Amer. Meteor. Soc.*, **93**, 1901-1912.

Tao, D., and F. Zhang, 2014: Effect of environmental shear, sea-surface temperature, and ambient moisture on the formation and predictability of tropical cyclones: An ensemble-mean perspective. *J. Adv. Model. Earth Syst.*, **6**, 384-404.

Tao, C. and H. Jiang, 2015: Distributions of shallow to very deep precipitation–convection in rapidly intensifying tropical cyclones. *J. Climate*, **28**, 8791-8824.

Tao, C., H. Jiang, and J. Zawislak, 2017: The relative importance of stratiform and convective rainfall in rapidly intensifying tropical cyclones. *Mon. Wea. Rev.*, **145**, 795-809.

Vigh, J.L., and W.H. Schubert, 2009: Rapid development of the tropical cyclone warm core. *J. Atmos. Sci.*, **66**, 3335-3350.

Wang, Y., Y. Li, and J. Xu, 2021. A new time-dependent theory of tropical cyclone intensification. *J. Atmos. Sci.*, **78**, 3855-3865.

Xu, J., and Y. Wang, 2015: A statistical analysis on the dependence of tropical cyclone intensification rate on the storm intensity and size in the North Atlantic. *Weather and Forecasting*, **30**, 692-701.

Xu, J., Y. Wang, and Z.M. Tan, 2016: The relationship between sea surface temperature and maximum intensification rate of tropical cyclones in the North Atlantic. *J. Atmos. Sci.*, **73**, 4979-4988.

Xu, J., and Y. Wang, 2018: Dependence of tropical cyclone intensification rate on sea surface temperature, storm intensity, and size in the western North Pacific. *Weather and Forecasting*, **33**, 523-537.

Xu, J., Y. Wang, and C. Yang, 2019: Interbasin differences in the median and variability of tropical cyclone MPI in the northern hemisphere. *J. Geophys. Res. Atmos.*, **124**, 13714-13730.

Zawislak, J., H. Jiang, G.R. Alvey, E.J. Zipser, R.F. Rogers, J.A. Zhang, and S.N. Stevenson, 2016: Observations of the structure and evolution of Hurricane Edouard (2014) during intensity change. Part I: Relationship between the thermodynamic structure and precipitation. *Mon. Wea. Rev.*, **144**, 3333-3354.

Zhang, F., and D. Tao, 2013: Effects of vertical wind shear on the predictability of tropical cyclones. *J. Atmos. Sci.*, **70**, 975-983.